C Journal of Carbon Research

MDPI

Article

Expanded Graphite (EG) Stabilization of Stearic and Palmitic Acid Mixture for Thermal Management of Photovoltaic Cells

Sereno Sacchet [1,*], Francesco Valentini [1], Alice Benin [2], Marco Guidolin [2], Riccardo Po [3] and Luca Fambri [1,*]

[1] Department of Industrial Engineering and INSTM Research Unit, University of Trento, Via Sommarive 9, 38123 Trento, Italy; francesco.valentini@unitn.it
[2] New Energies, Renewable Energies and Materials Science Research Center, Eni S.p.A., 30175 Marghera, Italy; alice.benin@eni.com (A.B.); marco.guidolin@eni.com (M.G.)
[3] New Energies, Renewable Energies and Materials Science Research Center, "Istituto Guido Donegani", Eni S.p.A., 28100 Novara, Italy; riccardo.po@eni.com
* Correspondence: sereno.sacchet@unitn.it (S.S.); luca.fambri@unitn.it (L.F.); Tel.: +39-0461-282413 (L.F.)

Abstract: In this work, passive cooling systems for the revamping of existent silicon photovoltaic (PV) cells were developed and analysed in order to mitigate the efficiency loss caused by temperature rise in the hot season. For this purpose, expanded graphite (EG) was used to stabilize a phase change material (PCM) with a melting temperature close to 53 °C in order to realize thermal management systems (TMSs) able to store heat at constant temperature during melting and releasing it in crystallization. In particular, stearic and palmitic acid mixture (PA-SA) was shape-stabilized in EG at different concentrations (10, 12 and 14 part per hundred ratio) under vacuum into a rotary evaporation apparatus followed by cold compaction; PA-SA leakage was reduced due to its intercalation between the graphite lamellae, and the thermal conductivity necessary to maximize the heat transfer to a bulk TMS was improved via powder cold compaction, which minimizes voids and creates preferential thermal conductive patterns. The composite materials, stable till 150 °C, were tested by differential scanning calorimetry (DSC) at 1 °C/min to precisely determine the phase transition temperatures and the enthalpic content, which was only slightly reduced from 196 J/g of the neat PCM to 169 J/g due to the very low EG fraction necessary for the stabilization. Despite only the 14:100 EG-to-PA-SA ratio, the system's thermal conductivity was enhanced 40 times with respect to the neat PCM (from 0.2 to 8.3 W/(m K), value never reached in works present in the literature), with a good convergence of the values evaluated through hot disk tests and laser flash analysis (LFA), finding correlation with both graphitic content and density. In order to completely avoid leaking with the consequent dispersion of PCM in the environment during the final application, all the samples were encapsulated in a PE-made film. The mechanical properties were evaluated with compression tests at 30 °C and 80 °C simulating a possible compressive stress deriving from the contact needed to maintain the TMS position on the rear of the PV cells. Finally, the material response was simulated by imposing thermal cycles into a climatic chamber and reproducing the three hottest and coldest days of summer 2022 of two Italian locations, Verona (Veneto, 45° N, 11° E) and Gela (Sicily, 37° N, 14° E), thus highlighting the thermal management effects with delays in temperature increase and daily peak temperature smoothing. The role of EG is strategic for the processing and the properties of the resulting composites in order to realize a proper compromise between the melting enthalpy of PCM and the thermal conductivity enhancement given by EG.

Keywords: expanded graphite; PCM composites; stearic acid; thermal conductivity; photovoltaic applications; thermal management

Citation: Sacchet, S.; Valentini, F.; Benin, A.; Guidolin, M.; Po, R.; Fambri, L. Expanded Graphite (EG) Stabilization of Stearic and Palmitic Acid Mixture for Thermal Management of Photovoltaic Cells. *C* **2024**, *10*, 46. https://doi.org/10.3390/c10020046

Academic Editor: Gil Goncalves

Received: 15 March 2024
Revised: 2 May 2024
Accepted: 10 May 2024
Published: 15 May 2024

1. Introduction

The excessive consumption of fossil fuels has led to an energy crisis and environmental issues like global warming, greenhouse gas emissions and ozone depletion. This has raised

demands for clean and renewable energy technologies to reduce dependency on fossil fuels. Solar energy is the most widely accepted renewable energy source due to its cleanliness, accessibility, sustainability and unlimited potential.

Photovoltaic modules (PVs) represent a clean and sustainable energy generation technology that has the capacity to grow. They absorb part of the sun's energy and dissipate the rest into heat. Module temperatures can rise due to excessive heat, which can shorten their lifespan and reduce their efficiency. The conversion efficiency of crystalline silicon solar cells decreases by 0.4–0.6% for each degree above the standard test conditions' temperature [1]. Therefore, it is essential to develop solar cell cooling systems (either active or passive [2]) in order to maintain the lowest possible working temperatures. Because active cooling requires the use of energy specifically dedicated to cooling the devices, passive cooling represents a more convenient approach.

Phase change materials (PCMs) are latent heat storage materials that absorb an incoming heat flux, liquefy when they reach the melting point, store a significant quantity of thermal energy and maintain a constant temperature. Likewise, when the temperature decreases, the material solidifies and releases the stored latent heat [3]. PCMs have several applications. First, they can be used as insulating materials in eco-sustainable architecture to improve the energy efficiency of buildings [4,5]. Thanks to the temperature control capacity, PCMs may be applied to batteries to avoid overheating [6] or on the back of photovoltaic (PV) modules as passive cooling systems [7,8]. In PV panels, they counterbalance the effect of the thermal coefficient [9], limit the decrease in power conversion efficiency and mitigate the degradation phenomena. PCM panels have also been proposed for low-temperature thermal storage [10]. From a chemical point of view, phase change materials can be divided in different classes [11].

Paraffins, fatty acids and poly(ethylene glycol) derivatives make up the family of organic PCMs. They are chemically stable and have a relatively high latent heat of fusion; paraffins do not exhibit the supercooling phenomenon and are not corrosive. On the other hand, they are expensive and have a low thermal conductivity. They are also flammable and exhibit a significant dimensional variability upon melting. Besides metals and alloys, salts and salts hydrated are the most representative inorganic PCMs. They are cheap, not flammable and have high thermal conductivity. The supercooling is an undesired characteristic of salt-based PCMs; they are also corrosive and have a poor stability. Furthermore, eutectic mixture (either organic–organic, inorganic–inorganic or organic–inorganic) allow for the fine tuning of the operating temperature of PCMs [12].

To solve the issue of low thermal conductivity in organic PCMs, the strategy of adding carbon (nano)materials has often been followed successfully [12]. Such carbon materials (graphene [13], graphene oxide [14], carbon nanotubes [15], expanded graphite [16]) have other benefits: besides increasing the thermal conductivity, they act as IR-antennae [11] and improve the heat absorption properties of the composite.

The main limitation of paraffinic PCMs is their confinement once molten, which can be solved with the use of macro- [17] or microencapsulation [18]. A third solution could be the shape stabilization of the PCM dispersing it into a matrix, as thermoplastic polymers [19,20], acrylic resins [21], styrene-(ethylene-co-butylene)-styrene triblock copolymer (SEBS) [22], ethylene propylene diene monomer (EPDM) rubber [23] or inorganic materials such as carbonaceous substances are able to improve thermal conductivity at the same time.

Carbon-based materials can rely on their excellent pore structure to efficiently absorb PCM, to prepare high-stability composite PCM [24]. As first choice candidates, graphene oxide products, notwithstanding some excellent properties, were discarded due to the high cost [11]. PCMs based on paraffins and expanded graphite (EG) have a special interest, thanks to the low density, high specific surface area, good chemical stability and the relatively low cost of raw materials compared to other low-melting matrices and carbon compound precursors [25,26], along with the stabilization effect that is able to limit leaking [27], which is favourable for the creation of thermal conductive networks within the shape-stabilized composite PCM [28]. The improvement of the thermal conductivity

of PCM-based systems is particularly important in order to allow fast charging and discharging rates that are critical issues when these materials are applied for the temperature management of electrical/electronic devices and batteries [29].

In the open literature, despite the existence of several works investigating the stabilization of PCMs within EG, the reported thermal conductivity values are generally low (from less than 1 W/(m K) [30,31] to 2.1 W/(m K) [32], rarely exceeding this value [29], along with the use of EG unless its fraction is higher than the PCM one [16]), and the PCM amount is limited to values below certain thresholds in order to avoid leaking (also below 70 wt.% [32]) with consequent complications in the production process and limitations in the use phase. In some works, thermal conductivity is enhanced only of less than 400% even with the addition of 20 wt.% EG [33].

Recently, fatty acid mixtures have been extensively studied in a wide variety of compositions [34–36], even if often their use in combination with EG excessively reduces the enthalpy of the composite material [37].

Based on these considerations, in this study, a novel EG vacuum impregnation method is reported for the shape stabilization of a bio-based mixture of stearic and palmitic acids (PA-SAs) used as PCMs. Cold compaction of the stabilized powder allows the enhancement of thermal conductivity by 40 times, using only 14 parts per hundred ratio (phr) of EG, guaranteeing high melting enthalpy (169 J/g), which is useful for the thermal management of electronic devices, with a particular focus on PV panels.

2. Materials and Methods

2.1. Materials

The selection of a PCM with a melting point in the range 50–60 °C was performed in order to make possible a thermal management action on silicon PV cells, avoiding a detrimental electrical conversion efficiency loss typical of the hottest summer days in Mediterranean regions.

The combination of fatty acids stabilized into EG was chosen due to the good interaction of these polar chains between the graphitic lamellae with respect to aliphatic chains as paraffin waxes, which provides good PCM stability above the melting point, in combination with the ability to provide a high thermal conductivity.

A vegetally originated fatty acid mixture of stearic (≥40 wt.%) and palmitic acids (≥50 wt.%), commercially named FATTY ACIDS C16-18 (PA-SA) provided by Carlo Erba Reagents (Val De Ruil, France), was selected as a PCM for its declared melting point (T_m) of 55 °C, discretely high melting enthalpy and sustainability offered by a bio-derived material.

The shape stabilization was performed using EG SIGRAFLEX® EXPANDAT provided by SGL CARBON GmbH (Meitingen, Germany).

In Table 1, the main thermophysical properties of the raw materials are summarized according to the producers' datasheets.

Table 1. Raw material thermophysical properties according to datasheets.

Raw Material	T_m [°C]	Density [g/cm^3]	Particle Size [µm]
PA-SA	55	0.890	-
EG	>600	0.025	4–40

In order to completely avoid PCM leakage, a polyethylene (PE) envelope with a thickness of 95 µm for alimentary applications provided by ORVET S.p.A. (Musile di Piave, Italy) was applied as the external envelope.

2.2. Sample Preparation

In this work, commercial raw EG was impregnated PA-SA adopting a one-step method. First, 10, 12 and 14 parts of EG per hundred PA-SA "matrix" were weighted and inserted

into a distillation flask. The mixture was manually stirred to obtain an initial dispersion of the two components. The mixture containing flask was then connected to a rotary evaporation apparatus (rotavapor) and both vacuum and rotation were applied, down to base vacuum levels (typically below 100 mbar). This operation was conducted at room temperature and had the main purpose of removing trapped air from the pores of the graphite and further disperse the components. Heat was then applied (90 °C) to the heat-carrying fluid (water) up to a full PA-SA melting point and the mixture was rotated under vacuum for 30 min at 20 rotations per minute (rpm). In Figure 1, the subsequent steps of the described preparative are schematically presented.

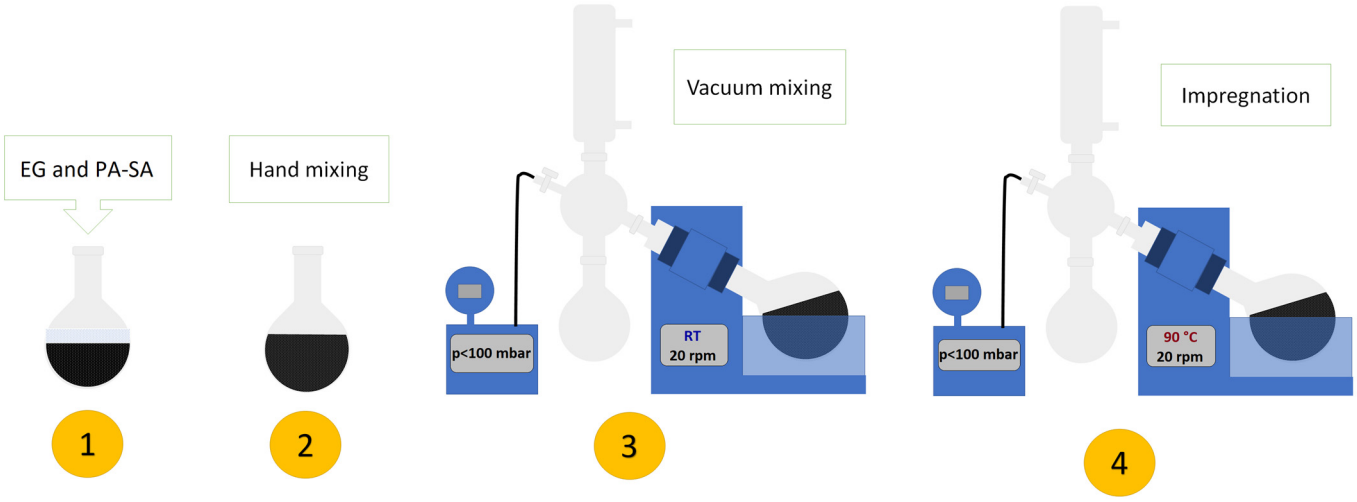

Figure 1. Schematic presentation of EG impregnation with PA-SA into rotavapor: (1) EG and PA-SA insertion into the flask; (2) EG and PA-SA hand mixing; (3) connection of the flask to the rotavapor and vacuum mixing at room temperature; (4) EG impregnation with molten PA-SA at 90 °C.

The rotavapor allows us to obtain a homogeneous composite PCM in powdery form even with a low-density filler like the EG used in this work. The intercalation of the PCM was obtained under vacuum conditions instead of the conventional procedures of melt impregnation through stirring [38–41], in which blocks of fixed densities are obtained after solidification.

The powders were then cold-compacted using a Carver® press, obtaining samples with sizes of 40 × 40 × 10 mm^3 and 63 × 63 × 20 mm^3. The selected method consisted of compaction at room temperature in order to avoid the squeezing of the molten PCM out of the porous matrix, applying variable pressures depending on the desired density. A pressure of 10 MPa had to be applied for at least 30 s to obtain a density of 0.94 g/cm^3, in order to permit the material to accommodate and plastically deform.

For the evaluation of the thermal energy storage capability described below, the PE film has been thermo-welded on prepared bricks using a thermo-welding machine ORVET VM-16 under vacuum. The advantage of applying the envelope around a shape-stabilized PCM is the limited volumetric expansion after the PCM melting; hence, there should be no ullage provided to guarantee better heat transfer and limited deformations and stresses to the PE film with respect to the macro-encapsulation of neat PCMs [42].

In Figure 2, the used mould with an internal dimension of 63 × 63 × 60 mm^3, a powder batch and two produced samples with a height measuring 20 mm, wherein the latter was vacuum-confined into the PE envelope, are reported in sequence.

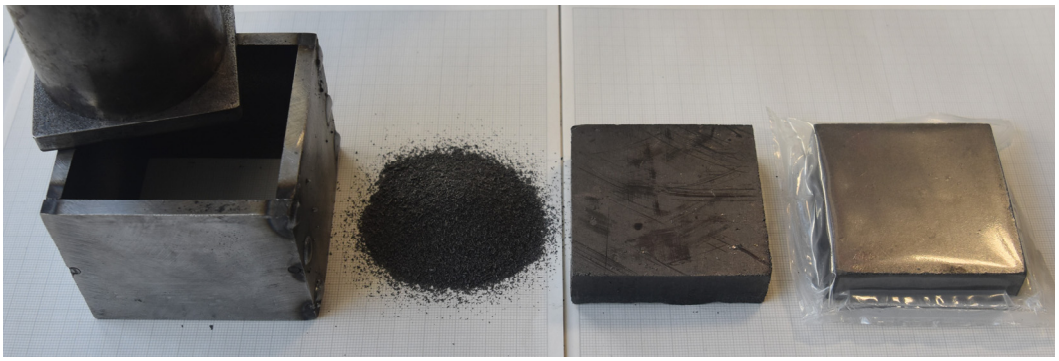

Figure 2. From left to right: Mould (63 × 63 × 60 mm^3) used for PA-SA/EG samples' production; powder before compaction; PA-SA/EG 14 phr sample (63 × 63 × 20 mm^3) produced via powder cold compaction; and enveloped PA-SA/EG 14 phr sample with thermo-welded PE film.

In Table 2, the samples considered for the full characterization and their composition are listed.

Table 2. Samples' coding and compositions.

Sample Code	PA-SA		EG	
	[phr]	[wt.%]	[phr]	[wt.%]
PA-SA/EG10	100	90.9	10	9.1
PA-SA/EG12	100	89.3	12	10.7
PA-SA/EG14	100	87.7	14	12.3

2.3. Experimental Metodologies

2.3.1. Raw Materials and Powder Characterization

Regarding the EG characterization, scanning electron microscopy (SEM) observation of the powder was performed using a Jeol IT300 microscope (Tokyo, Japan) equipped with a secondary electron (SE) detector and working at an acceleration voltage of 20 kV.

The tap density (ρ_{tap}) of the EG was evaluated by weighing the mass contained in a 500 mL container using a Kern (Balingen, Germany) PNJ600-3M balance (sensitivity 0.001 g) and performing 5 measurements of different specimens.

The apparent density (ρ_{app}) measurements of the neat PA-SA and impregnated powdery mixtures were conducted using an AccuPycII 1330 helium pycnometer (Micrometrics Instrument Corporation, Norcross, GA, USA) operating at a temperature of 23 °C. For each sample, 30 measurements were performed using a testing chamber of 1 cm^3. The theoretical density (ρ_{th}) was evaluated by considering the weight fractions of the phases as well as the phase density, the PA-SA measured density and a reference value of 2.26 g/cm^3 for graphite [43].

The void fraction (ϑ_v) was calculated using Equation (1):

$$\vartheta_v = \frac{\rho_{th} - \rho_{app}}{\rho_{th}} \cdot 100 \quad (1)$$

The thermogravimetric analysis (TGA) of all the materials was performed in a temperature interval between 30 °C and 700 °C, at a heating rate of 10 °C/min through a Mettler TG50 thermobalance (Mettler-Toledo, Greifensee, Switzerland) in the presence of nitrogen or air flow of 100 mL/min, using an alumina crucible. The specimen masses were 2.5 mg for EG and 20 mg for the other samples. The onset of the thermal degradation (T_{onset}) was determined as the point at which the derivative of the TGA (DTGA) corresponds to 0.01%/°C. The temperature associated with a mass loss of 5 wt.% ($T_{5\%}$) and the temperature associated with the maximum rate of degradation (T_{peak}) were also determined. Moreover,

weight fractions at 200 °C (m_{200}), 500 °C (m_{500}), 600 °C (m_{600}) and the residual mass at 700 °C (m_{700}) were reported.

Differential scanning calorimetry (DSC) tests were performed using a Mettler DSC30 calorimeter (Mettler-Toledo, Greifensee, Switzerland). The neat PA-SA was preliminary tested at three different rates (0.1 °C/min, 1 °C/min and 10 °C/min) in the range 20–75 °C in order to determine the best velocity to precisely appreciate the transition enthalpies and temperatures, selecting 1 °C/min for the characterization of the composite samples. The tests were performed under a nitrogen flow of 100 mL/min with a thermal cycle of heating/cooling/heating in the range 40 °C to 60 °C into aluminium crucibles having 40 µL volume. The melting temperatures during the first and the second heating scan (T_{m1} and T_{m2}), the crystallization temperature (T_c) in cooling and the specific melting and crystallization enthalpy values (ΔH_{m1}, ΔH_c and ΔH_{m2}) were obtained. The effective PCM content of the specimens was determined by considering the second heating scan (PCM_{m2}^{eff}) as the ratio between the specific enthalpy of the specimens and the corresponding specific enthalpy values of the neat PCM, as shown in Equation (2), while in Equation (3), the calculation for the efficiency of melting (η_{m2}) during the second melting scan is reported:

$$PCM_{m2}^{eff} = \frac{\Delta H_{m2}}{\Delta H_{m2,PCM}} \cdot 100 \quad (2)$$

$$\eta_{m2} = \frac{\Delta H_{m2}}{\Delta H_{m2,PCM} \cdot W_{PCM}} \cdot 100 \quad (3)$$

where ΔH_{m2} and $\Delta H_{m2,PCM}$ are, respectively, the specific enthalpy values associated with melting during the second heating scan of the sample and neat PCM, while W_{PCM} is the weight fraction of the PCM. The results were reported considering both the theoretical weight fraction of PA-SA and those derived from TGA.

2.3.2. Plates' Characterization

The ability of the compacted plates to retain PCM was investigated through leaking tests of disks or plates, consisting in monitoring the mass of specimens placed into an oven at 60 °C as a function of time. A preliminary test for having direct comparison with works present in the literature [24,30,44] was conducted to small disks of 20 mm diameter, 1 mm thick (surface-to-volume ratio 8.2 mm^{-1}) and 1 g of mass on filter paper for 5 h, quantifying the specimens' weight loss after 30 min, 60 min, 90 min and at the end of the 5 h. The second test was conducted using 110 × 110 × 3 mm^3 plates (surface-to-volume ratio 7.0 mm^{-1}) with masses of 30 g on an absorbent paper towel for a period of 40 days. In this case, the residual PCM content was calculated as the weight fraction with respect to the total specimen weight. The relative loss fraction (f) was determined as the ratio between weight loss (Δ%) and PCM content (Equation (4)) and it was also normalized (f^*) to the EG content (EG%), as shown in Equation (5):

$$f = \frac{\Delta\%}{\text{PCM content}} \quad (4)$$

$$f^* = \frac{f}{\text{EG\%}} \quad (5)$$

At the beginning of the test, the theoretical PCM contents in Table 2 were assumed and the weight losses with time were totally associated with PCM leakage.

The fracture surfaces of the compacted plates were observed using a Zeiss Supra 40 (Carl Zeiss, Oberkochen, Germany) field emission scanning electron microscope equipped with an SE detector and working at an acceleration voltage of 2.5 kV. Before the observations of the fractured surfaces, the specimens were metallized through the deposition of a thin electrically conductive coating of Pt-Pd inside a vacuum chamber.

Thermal conductivity (λ) was determined as the product between specific heat capacity (c_p), thermal diffusivity (α) and bulk density (ρ) as reported in Equation (6):

$$\lambda = \alpha \cdot \rho \cdot c_p \quad (6)$$

The specific heat capacity was determined following ASTM E1269-11 standard [45]. Three specimens for each sample were tested with a Mettler DSC30 machine, performing thermal cycles consisting of 4 min of isotherm at 20 °C, heating at 5 °C/min from 20 °C to 90 °C and another 4 min of isotherm at 90 °C. By comparing the DSC curves obtained from testing a sapphire reference of known specific heat capacity, the c_p of the samples at 30 °C (c_{p30}) and 80 °C (c_{p80}) were determined.

The thermal diffusivity was determined using two different instrumentations:

- A Neztsch Analysing & Testing (Selb, Germany) laser flash analyser (LFA) 446 on specimens having disk shapes and dimensions measuring 12.7 mm in diameter and 3 mm in thickness, obtained via cold compression. The tests were carried out at a 30 °C, imposing laser signals of 250 V for a pulse width of 0.6 ms.
- A hot disk thermal analyser (Hot Disk Instruments, Göteborg, Sweden), equipped with a 7577 sensor (diameter of 4.002 mm), according to ISO 22007 standard [46] on specimens with a disk shape and dimensions of 20 mm in diameter and 5 mm in thickness, inserted into a Memmert HCP climatic chamber (Schwabach, Germany) at 30 °C and controlled relative humidity fixed at a value of 30%, with an application of 80 mW of power for 1 s. These operating parameters were chosen in order to guarantee a thermal increase of at least 2 °C for each specimen, as reported in the standard. At least three measurements were performed for each sample.

The bulk density was evaluated as the ratio of the weighted disks using a Kern PNJ600-3M balance (sensitivity 0.001 g) and the volume computed measuring their dimensions with a calliper having 0.01 mm of sensitivity. In order to distinguish the thermal conductivity values measured with the two different techniques, the symbols λ_{HD} and λ_{LFA} were introduced to refer, respectively, to the hot disk and LFA tests. Measurements above the PA-SA melting temperature were not possible due to the leaking problems of the composite material.

In order to obtain practical information regarding the efficacy of the prepared bricks for the thermal management of PV systems, tests simulating reached temperatures by the PV cells were performed. PE-encapsulated specimens of masses 12 g (A), 66 g (B) and 92 g (C) were tested using a climatic chamber (model DM340C by Angelantoni Industrie S.r.l., Massa Martana, Italy), simulating the material response during the three hottest and coldest days of summer 2022 of two different Italian locations, Verona (Veneto, 45° N, 11° E) and Gela (Sicily, 37° N, 14° E). The thermal cycles were set, reproducing the temperatures reached by the panel (T_p, Equation (7) [47]) with an inclination of 30° with respect to the horizontal, imposing temperature steps with a duration of one hour.

$$T_p = T_a + K \cdot \phi \quad (7)$$

where T_a is the ambient temperature, K is a coefficient between 0.025 and 0.030 and ϕ is the incident irradiation in the same plane as the PV panel. The data of T_a and ϕ hour by hour for all of summer in 2022 were provided by ARPAV (Agenzia Regionale per la Prevenzione e Protezione Ambientale del Veneto) [48] for Verona and SIAS (Servizio Informativo Agrometeorologico Siciliano, Regione Sicilia) [49] for Gela. The adopted K parameter was 0.029, selected reversing Equation (7) using T_p, T_a and ϕ data for a real Sicilian case. The chamber was programmed by setting 72 h long cycles composed of 1 h increments, preceded by 2 h of isotherm at the starting temperature of the cycles. In Figure 3a–d, the temperature profiles of air and panel (using Equation (7)) at tilt angles of 0° and 30°—common values of the application conditions to optimize the incoming irradiance—are reported.

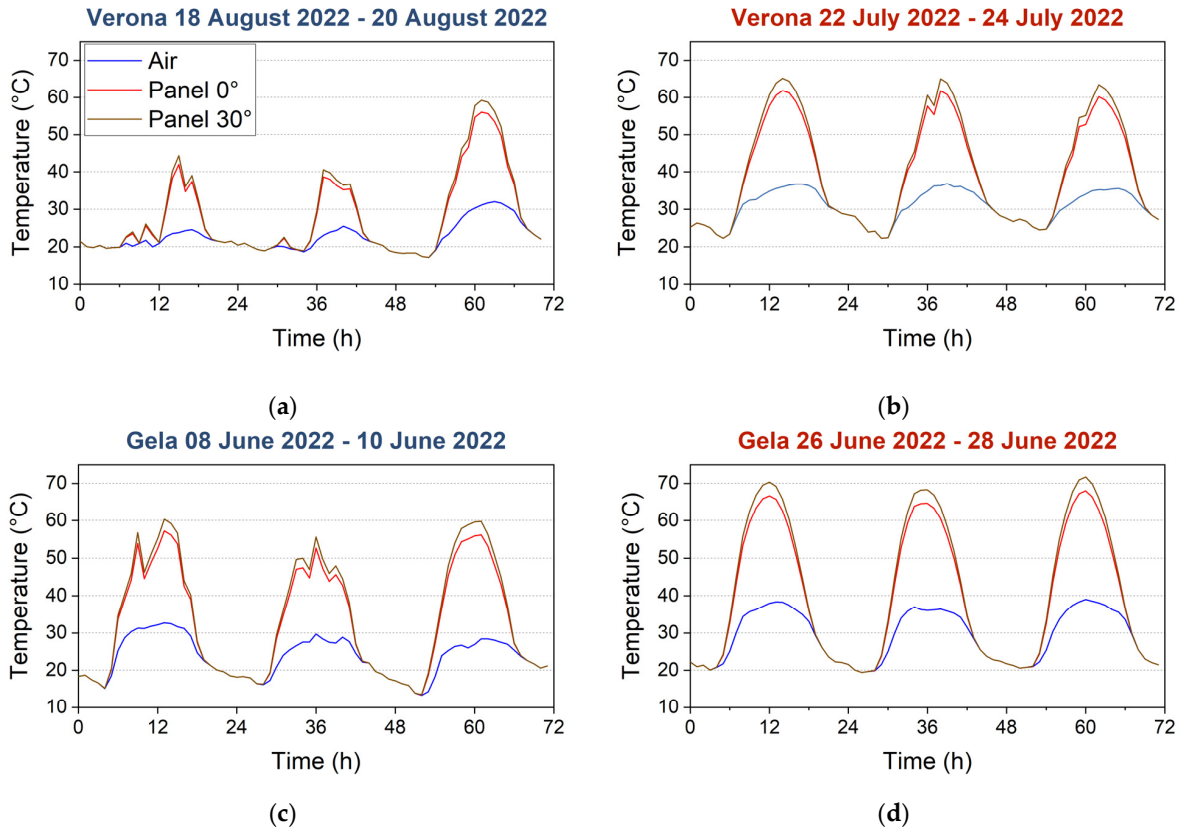

Figure 3. Set temperature profiles of: (**a**) three coldest days in Verona [48]; (**b**) three hottest days in Verona [48]; (**c**) three coldest days in Gela [49]; (**d**) three hottest days in Gela [49].

The simulating temperatures inside the climatic chamber were those of the panel inclined at 30°, thus constituting the worst situation in terms of temperature increment as well as the most common one. The temperature was recorded every 30 s using an OM-HL-EH-TC Temperature Datalogger (Omega Engineering, Norwalk, CA, USA) equipped with type-K thermocouples (resolution 0.1 °C): three thermocouples were located on the surfaces of the specimens and one in the air in order to record the temperature profile of the climatic chamber. The specimens were put on the surface of a glass in order to simulate the real working conditions of the materials in a PV panel. In Figure 4, the testing configuration of samples and thermocouples is reported.

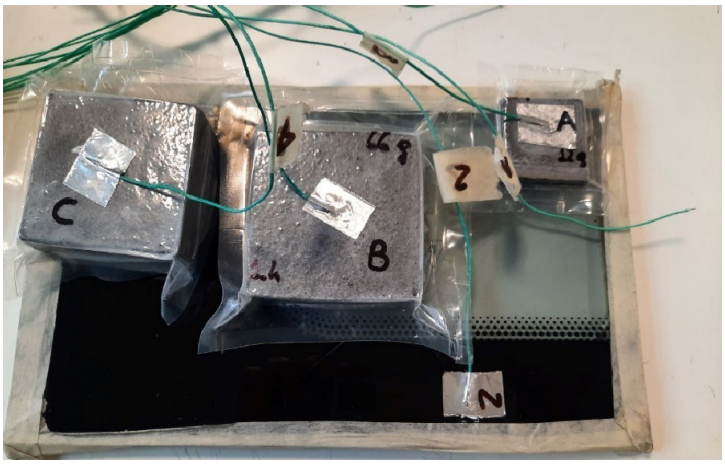

Figure 4. Samples tested inside the climatic chamber: (**A**) (12 g, 9.4 kg/m^2 surface density), (**B**) (66 g, 5.3 kg/m^2), (**C**) (92 g, 3.8 kg/m^2).

The mechanical behaviour was evaluated through compression tests using an Instron (Pianezza, Italy) 5969 testing machine equipped with a load cell of 10 kN and a climatic chamber. PE-encapsulated specimens of dimensions 40 × 40 × 10 mm^3 were tested, both at 30 °C and at 80 °C, at a rate of 1 mm/min. From the obtained stress–strain curves, the compressive modulus of elasticity (E_C) in the linear part of the curve between 7% and 10% of strain and the stress at 10% of deformation (σ_{10}) were evaluated for both the tests at 30 °C and 80 °C. For the tests at 30 °C, the strain at 5 MPa of stress (ε_5) was computed, while for the tests at 80 °C, the strain at 0.5 MPa ($\varepsilon_{0.5}$) was selected due to the different response of the specimens in function of the temperature. Furthermore, the stress at 20% of deformation (σ_{20}) was evaluated at 80 °C.

3. Results and Discussion

3.1. SEM Observations of EG before Impregnation

In Figure 5, the micrographs of the EG at different magnifications are reported.

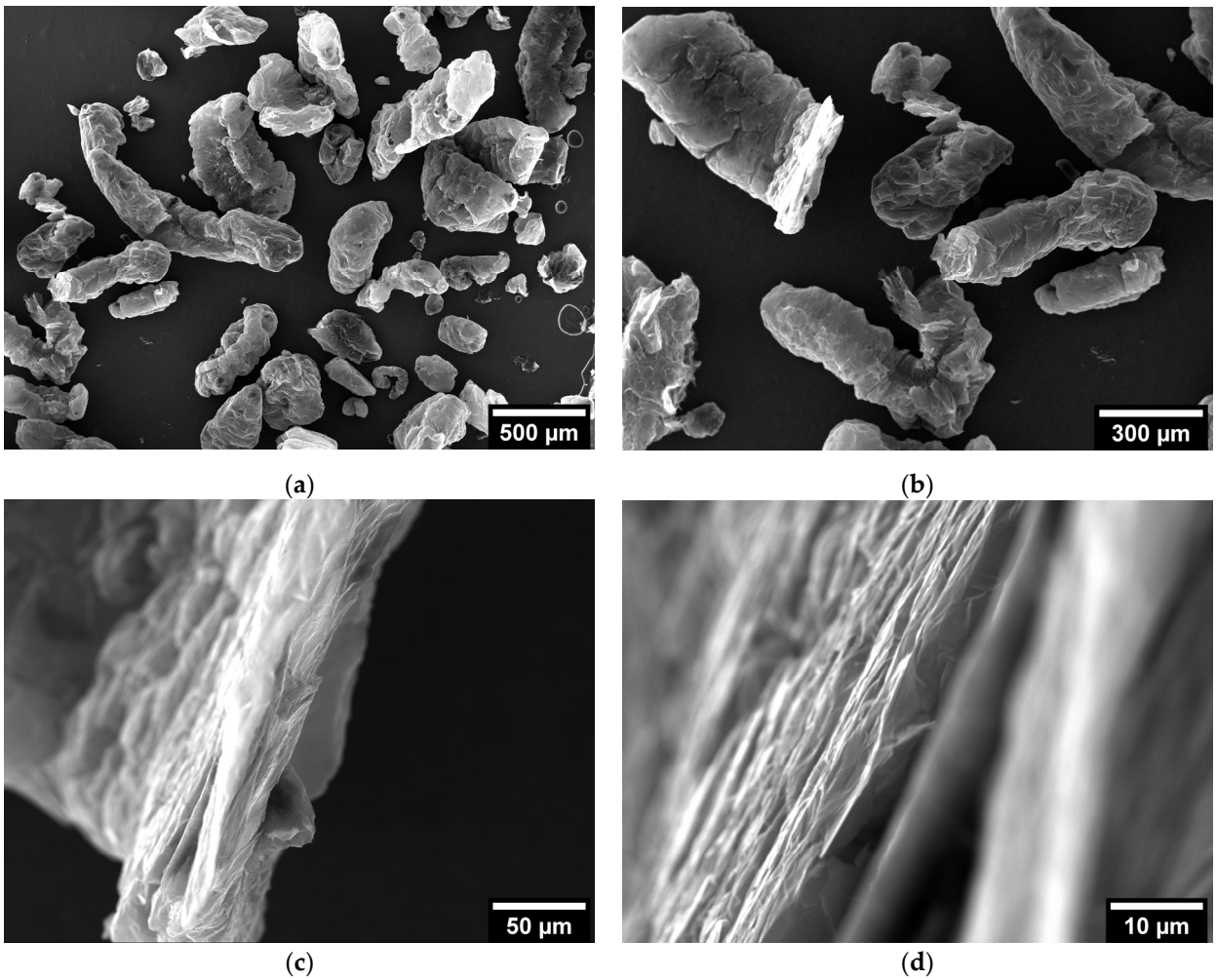

(**a**) (**b**) (**c**) (**d**)

Figure 5. SEM micrographs of EG powder: (**a**) granules' overview; (**b**) detailed granules' geometry and morphology; (**c**) side view of a single granule; (**d**) lamellar graphitic structure detail.

The typical worm-like structure [24,39,50] is recognizable, with longitudinal and transversal dimensions computed from Figure 5a, respectively, of 840 ± 270 µm and 280 ± 110 µm, having a broad particle size distribution typical of EG. The tap density of the powdery EG was 0.031 ± 0.001 g/cm^3, which is slightly higher than that specified by the producer's datasheet. The EG under investigation can be considered quite coarse and less expanded compared with the one used by Yu et al. in a similar work (80 meshes,

600 mL/g expandable volume) [51], while the dimensions are similar to those used by Liu et al. (50 meshes) [50]. The morphology is quite different to that of the more rounded EG produced by Tian et al., characterized by V-type open or semi-open interconnected pores on the surface, whose pore sizes range from dozens of microns to hundreds of microns, even if the granular dimension is comparable [52]. The skeleton density evaluated with helium pycnometer was 2.268 ± 0.004 g/cm^3, in accordance with graphite theoretical density (2.26 g/cm^3) [43].

3.2. Density Measurements

In Table 3, the density values measured for neat PA-SA and powdery impregnated samples are listed. Moreover, a comparison with the theoretical density values, accompanied to the values of void fraction are reported.

Table 3. Densities and void fractions of neat PA-SA and EG-stabilized systems.

Sample	ρ_{app} [g/cm^3]	ρ_{th} [g/cm^3]	ϑ_v [wt.%]
PA-SA	0.945 ± 0.007	-	-
PA-SA/EG10	0.919 ± 0.013	1.065 ± 0.006	13.7 ± 1.3
PA-SA/EG12	0.807 ± 0.012	1.086 ± 0.006	17.8 ± 1.2
PA-SA/EG14	0.701 ± 0.008	1.107 ± 0.006	36.7 ± 0.9

In Figure 6, the trend of theoretical and experimental density for PA-SA/EG powders in the function of the EG content is reported.

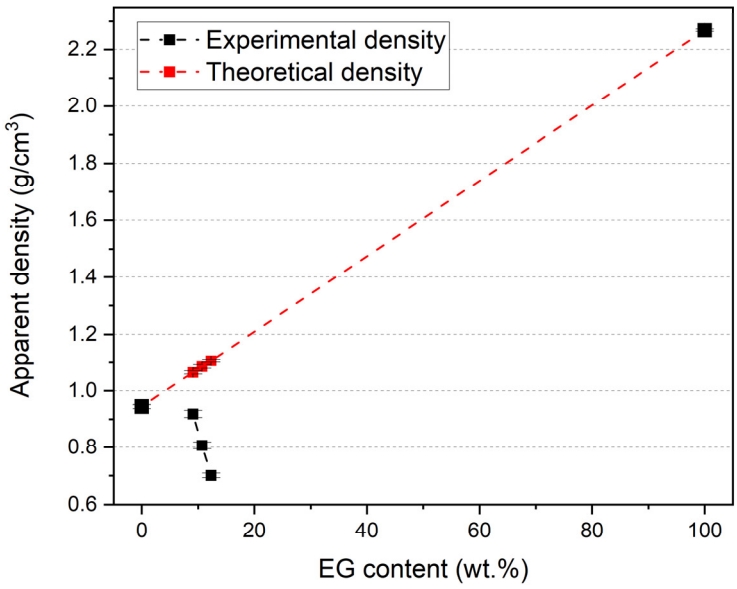

Figure 6. Apparent density trend of PA-SA/EG powder in function of EG content.

A decrease in system density increases the EG content, which is opposite to the trend shown from the theoretical density, with a consequent increase in void fraction. This trend can be explained due to the highly porous nature of EG, which behaves as a matrix in which the PA-SA can intercalate, remaining entrapped due to the action of capillary forces, surface tension and physical interaction [24,41,53]. These powders are then compacted for panel realization, reaching higher densities and reducing intergranular porosity.

The powder density is an important parameter to be considered in the cold compaction operation since it influences the mould volume, which also needs to be adjusted depending on the selected EG content, final required density and final thickness.

3.3. Thermogravimetric Analysis (TGA)

In order to investigate the material stability in temperature, thermogravimetric analysis was performed. In Figure 7, the TGA curves in nitrogen of neat PA-SA, EG and samples investigated as residual mass and derivative of weight loss (DTGA) are reported, while in Table 4, the characteristic temperatures and weight fractions are listed.

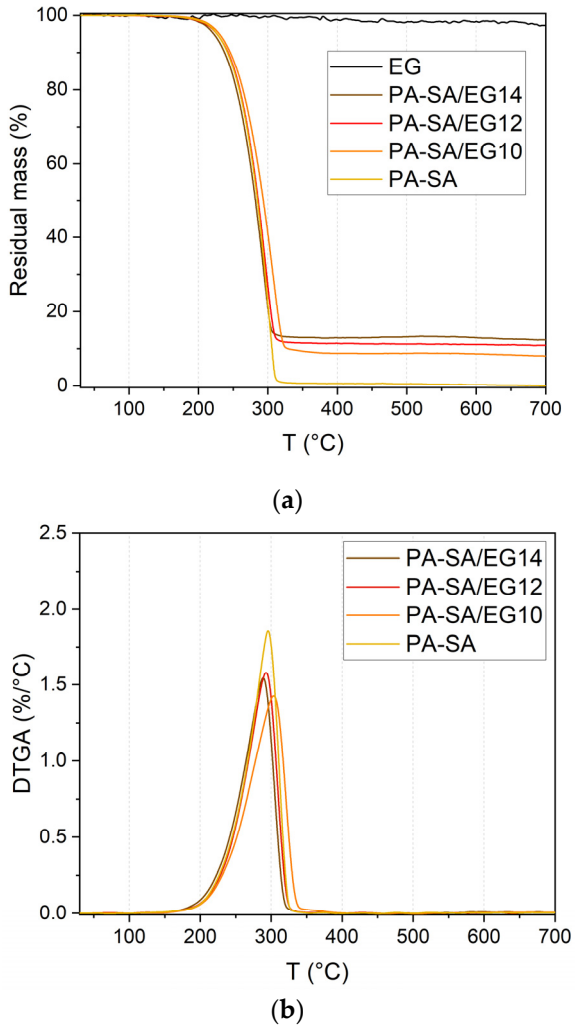

Figure 7. TGA curves in nitrogen atmosphere: (**a**) residual mass; (**b**) derivative of mass loss (DTGA).

Table 4. Selected results of TGA and DTGA analyses in nitrogen.

Sample	T_{onset} [°C]	$T_{5\%}$ [°C]	T_{peak} [°C]	m_{200} [wt.%]	m_{500} [wt.%]	m_{600} [wt.%]	m_{700} [wt.%]
PA-SA	153	226.8	295.4	98.7	0.5	0.3	0.0
PA-SA/EG10	156	230.2	303.6	98.9	8.7	8.6	8.0
PA-SA/EG12	160	226.7	292.7	98.5	11.2	11.1	10.9
PA-SA/EG14	159	222.3	288.7	98.3	13.2	12.9	12.3
EG	-	-	-	99.1	98.4	98.3	97.3

PA-SA starts the degradation at about 153 °C, reaching relatively complete degradation at 400 °C with the absence of any residue at the end of the tests. In the case of composite materials, the values of T_{onset}, $T_{5\%}$ and T_{peak} are similar to the neat PCM even though the derivative of the mass loss presents a less pronounced peak due to the stabilization effect of the EG. Some mass residue remains in all the three compositions (8.0 wt.%, 10.9 wt.% and 12.3%), proportionally to the theoretical fraction of EG (9.1 wt.%, 10.7 wt.% and 12.3 wt.%)

in accordance with other studies in PCM/EG systems [30]. The residues slightly differ from the predicted values due to probable inhomogeneities derived from the small specimens considered and the weight loss of the EG itself. Nonetheless, EG presents stability in both atmospheres till 700 °C, compared to that produced by Tiang at al., which presents weight loss higher than 30 wt.% at 700 °C and a degradation onset at around 70 °C [52]. This indicates that the EG used in this work was probably pretreated at a temperature comparable or higher than 700 °C.

3.4. Differential Scanning Calorimetry (DSC)

The selection of the most suitable rate to determine the phase transition temperature was performed comparing the DSC curves obtained testing the neat PCM at three different rates, as reported in Figure 8. In order to appreciate, in comparable scales, the peak shapes and positions, the curves obtained at 1 °C/min and 0.1 °C/min were normalized by multiplying, respectively, a factor of 5 and 25 with respect to the heat flux signal at 10 °C/min.

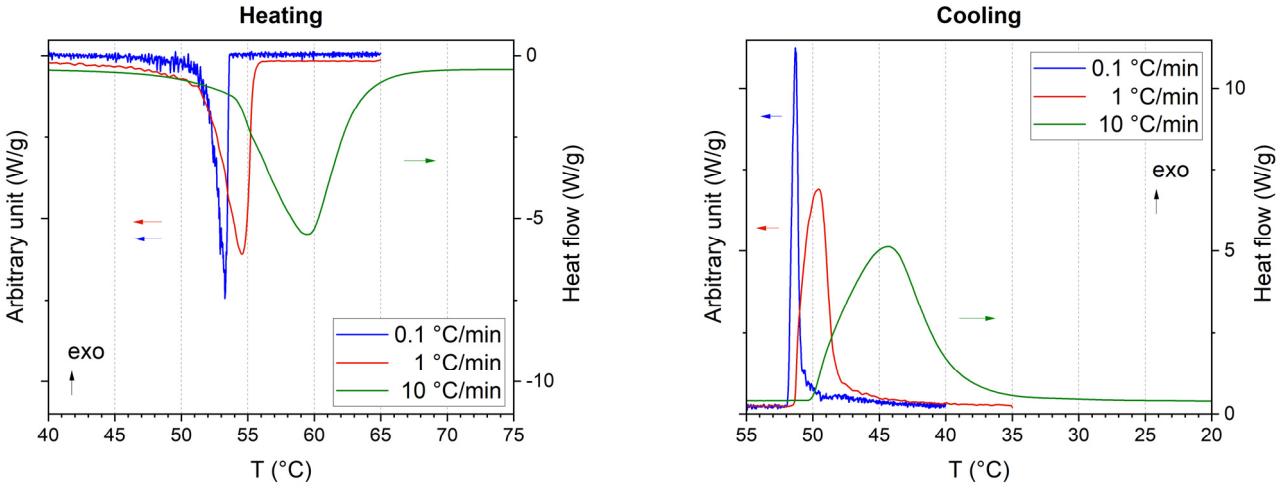

(**a**) (**b**)

Figure 8. DSC thermograms of neat PA-SA at different rates: (**a**) heating scan; (**b**) cooling scan.

The lower the scanning rate, the narrower the interval of transitions, in particular, about 3, 7 and 12 degrees, for 0.1, 1 and 10 °C/min, respectively. Moreover, a shift in the transition temperatures can be noticed, which is a consequence of thermal inertia effects increasing at higher scanning rates. Melting peaks were registered at 53.3, 54.6 and 59.6 °C after heating at 0.1, 1 and 10 °C/min, respectively. The slower the heating (cooling) ramp, the more precise the evaluation of transition temperature range and peak due to the similarity to real environmental conditions that involve very slow transitions (~0.01 °C/min). At 0.1 °C/min, the thermogram is too noisy to guarantee a precise integration to quantify the enthalpy. For these reasons, 1 °C/min was selected as the scanning rate for the thermal characterization of the systems for the most precise possible determination of transition temperatures and enthalpy, as comprehensively explained by Valentini et al. [54].

The DSC curves of neat PA-SA and samples tested at 1 °C/min are reported in Figure 9 and the main results are summarized in Table 5.

The melting temperature of 53.4 °C of the PA-SA mixture indicates that the composition is closed to the eutectic one, with a PA-to-SA mass ratio ranging from 58.8 to 41.2 and a melting temperature of 53.2 °C, as evaluated using Schroder's equation by Zhang et al. [44], which lowers the melting point of both PA (61.99 °C) and SA (68.54 °C) even if the melting enthalpy is higher (196.1 J/g vs. 178.1 J/g), but which is nonetheless lower than the single aliphatic acid, i.e., neat PA (198.4 J/g) and SA (201.8 J/g) [44].

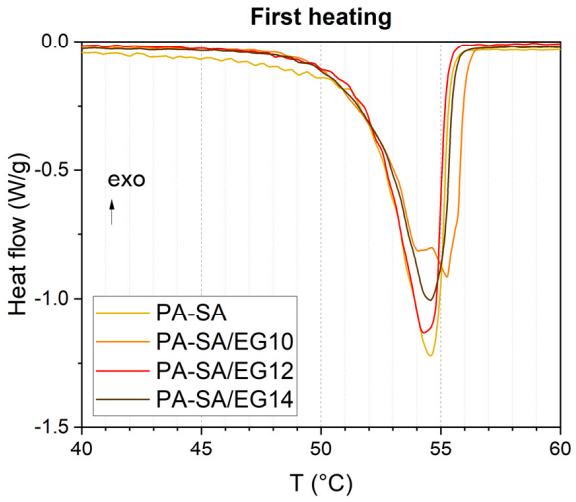

(**a**)

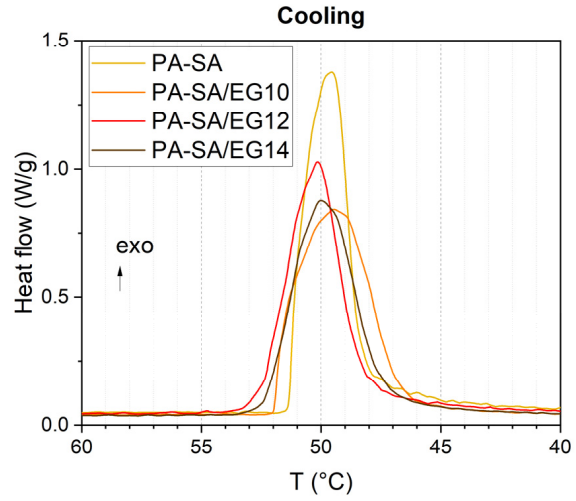

(**b**)

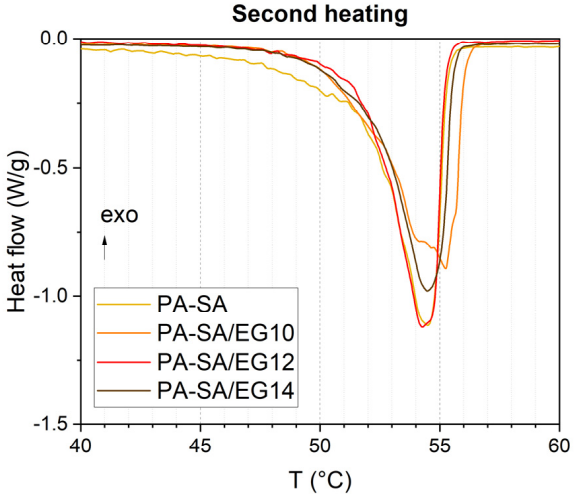

(**c**)

Figure 9. DSC thermograms of the neat PA-SA and PA-SA/EG systems at 1 °C/min: (**a**) first heating scan; (**b**) cooling scan; (**c**) second heating scan.

Table 5. Results of DSC tests at 1 °C/min using 40 µL crucibles.

Sample	T_{m1} [°C]	ΔH_{m1} [J/g]	T_c [°C]	ΔH_c [J/g]	T_{m2} [°C]	ΔH_{m2} [J/g]	PCM_{m2}^{eff} [wt.%]	η_{m2} [wt.%]	η_{m2} * [wt.%]
PA-SA	53.4	195.4	50.9	193.3	53.4	196.1	100	100	100
PA-SA/EG10	54.5	180.0	50.2	179.5	54.5	180.9	92.3	101.5	100.3
PA-SA/EG12	53.4	175.7	50.9	172.9	53.4	176.0	89.8	100.5	100.7
PA-SA/EG14	53.7	168.6	50.8	168.0	53.6	168.7	86.0	98.1	98.1

* Efficiency evaluated considering as EG weight fraction the residues at 700 °C from TGA.

The stabilization of the PCM using EG has almost no influence on its thermal properties; as reported in Table 5, the melting and crystallization temperatures are very closed, as well as the thermogram profiles. Transition enthalpies and temperatures are coherent to those evaluated in many studies [24,25,39].

The melting enthalpies are coherent with those predicted considering the EG weight fraction, with differences from 0.5 to 2 wt.% (η_{m2}) that could be attributed to any inhomogeneity of the systems. With 14 phr of EG content, the melting enthalpy is reduced to 168.9 J/g, which corresponds to 86% of the neat PA-SA value.

The crystallization enthalpy values are lower than those of melting due to the impossibility for the PCM to completely crystallize with the consequent presence of a few remaining amorphous regions, even if this effect should be reduced due to the heterogeneous nucleation enhancement provided by EG, which acts as a nucleating agent [24]. The crystallization temperatures are slightly lower in comparison with the melting ones due to the energy barrier that must be overcome for both melting in heating and crystallizing in cooling, accompanied with thermal inertia effects which cannot be completely neglected.

3.5. Leaking Test

Moving on to compacted system characterization, the ability to retain the PCM above the melting point was evaluated by performing leaking tests, whose results are reported in Figure 10, expressing the total mass loss for the short test and residual PCM content as a function of time for the long one. In Table 6, EG content (EG%), weight loss (Δ%), relative loss fraction (f), its normalized value (f*) and its reciprocal value are reported. This last parameter can be considered as an efficiency in leakage reduction, which refers to the short leaking test.

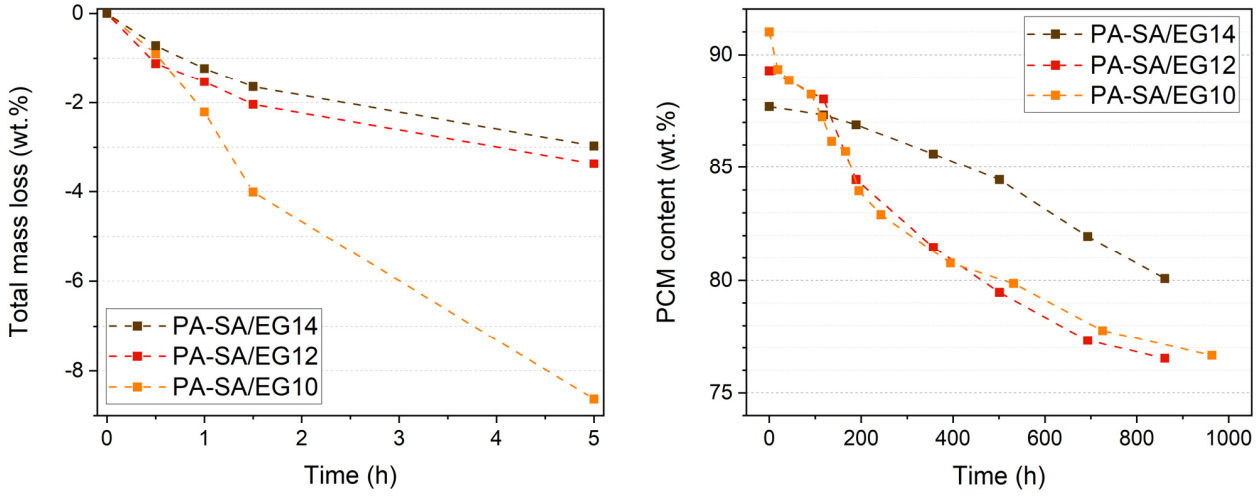

(**a**) (**b**)

Figure 10. Results of leaking tests at 60 °C: (**a**) total mass loss of disks 20 mm in diameter and 3 mm thick in short test; (**b**) PCM residue of plates with dimensions measuring 110 × 110 × 3 mm^3 in long test.

Table 6. Parameters for the determination of the efficiency in leakage reduction, referring to the 5-h long test, of disks with a surface-to-volume ratio (S/V) of 8.2 mm^{-1}.

Sample	EG% [wt.%]	Δ% [wt.%]	f [wt.%]	f^* [-]	$1/f^*$ [-]
PA-SA/EG10	9.1	8.6	9.5	1.04	1.0
PA-SA/EG12	10.7	3.3	3.8	0.35	2.8
PA-SA/EG14	12.3	2.9	3.4	0.28	3.6

From the short test, the beneficial effect of increasing the EG content in the PCM stability can be observed, limiting the mass loss from 8.6 wt.% to 2.9 wt.% passing from 10 phr to 14 phr of EG content in 5 h with an improvement of the $1/f^*$ parameter, respectively, from 1.0 to 2.6 and 3.6, with a drastic loss reduction at only 12 phr. Despite the fact that the shape of the tested disks was well maintained, the mass losses in some cases were higher than those obtained in similar works presented in the literature. Zhang et al. [44], with only 8.3 wt.% EG, obtained only 1 wt.% of mass loss after 1 h of pretreating the EG in a microwave oven, a result that in the present work was not even obtained at 12.3 wt.% EG. Another study shows that with 9 wt.% EG (close to the fraction of the PA-SA/EG10 sample), the leakage can also be completely avoided after 5 h [50].

The leakage performances are nevertheless comparable with respect to that obtained by Ao et al. (−1 wt.% after 30 min adding 12 wt.% of EG) [24] and are also better in comparison with those by Liu et al. (−5 wt.% in 90 min after vacuum impregnation with 12 wt.% of EG) [30].

In Table 7, the same parameters evaluated for the test, within a 40-day duration, are reported.

Table 7. Parameters for the determination of the efficiency in leakage reduction, referring to the 40-day test of plates with a surface-to-volume ratio (S/V) f 7.0 mm^{-1}.

Sample	EG% [wt.%]	Δ% [wt.%]	f [wt.%]	f^* [-]	$1/f^*$ [-]
PA-SA/EG10	9.1	14.3	15.8	1.73	0.6
PA-SA/EG12	10.7	12.8	14.3	1.34	0.8
PA-SA/EG14	12.3	7.6	8.7	0.71	1.4

Looking at the results of the longer test, the continuous PCM loss, which is much less pronounced at 14 phr content, is observable. After an initial intense leakage of the PA-SA/EG10 sample, the trends at 10 and 12 phr were similar with the double PCM loss (−14.3 wt.% and −12.8 wt.%) in comparison with the PA-SA/EG14 sample (−7.6 wt.%). An EG content of 14 phr can be thus considered the minimum amount to stabilize PA-SA (also, in this case, the highest $1/f^*$ value), probably because with lower contents, the interlamellar space is not sufficient to retain all the PCM. Gao et al., using higher amounts for a further stabilization effect, reached no leakage at all (without application of pressures) at 20 wt.% of EG content [25], while Fang et al. observed no leakage at only 17 wt.% after microwave EG expansion [38]. Observing the trend of Figure 10b, a probable threshold to stop the PA-SA loss can be at around 25 wt.% of EG, which is more than the double contained in the PA-SA/EG14 sample. A compromise adopted to maximize PA-SA content using the minimum possible amount of EG to stabilize it is the selection for the 14 phr EG, which also reflects the best thermal conductivity improvement.

A practical solution to completely avoid leakage without an excessive decrease in the PCM content of the composite is the encapsulation using the PE envelope film.

Alternatively, a solution could be the use of another piece of graphite or try to pretreat it to further expand the graphite (with a microwave oven [44] or via thermal treatment in a muffle [53]).

3.6. Scanning Electron Microscopy (SEM) Observation

In Figure 11a–f, SEM micrographs of the fracture surfaces of compacted samples before PA-SA melting (left) and after at least one melting cycle (right) are shown.

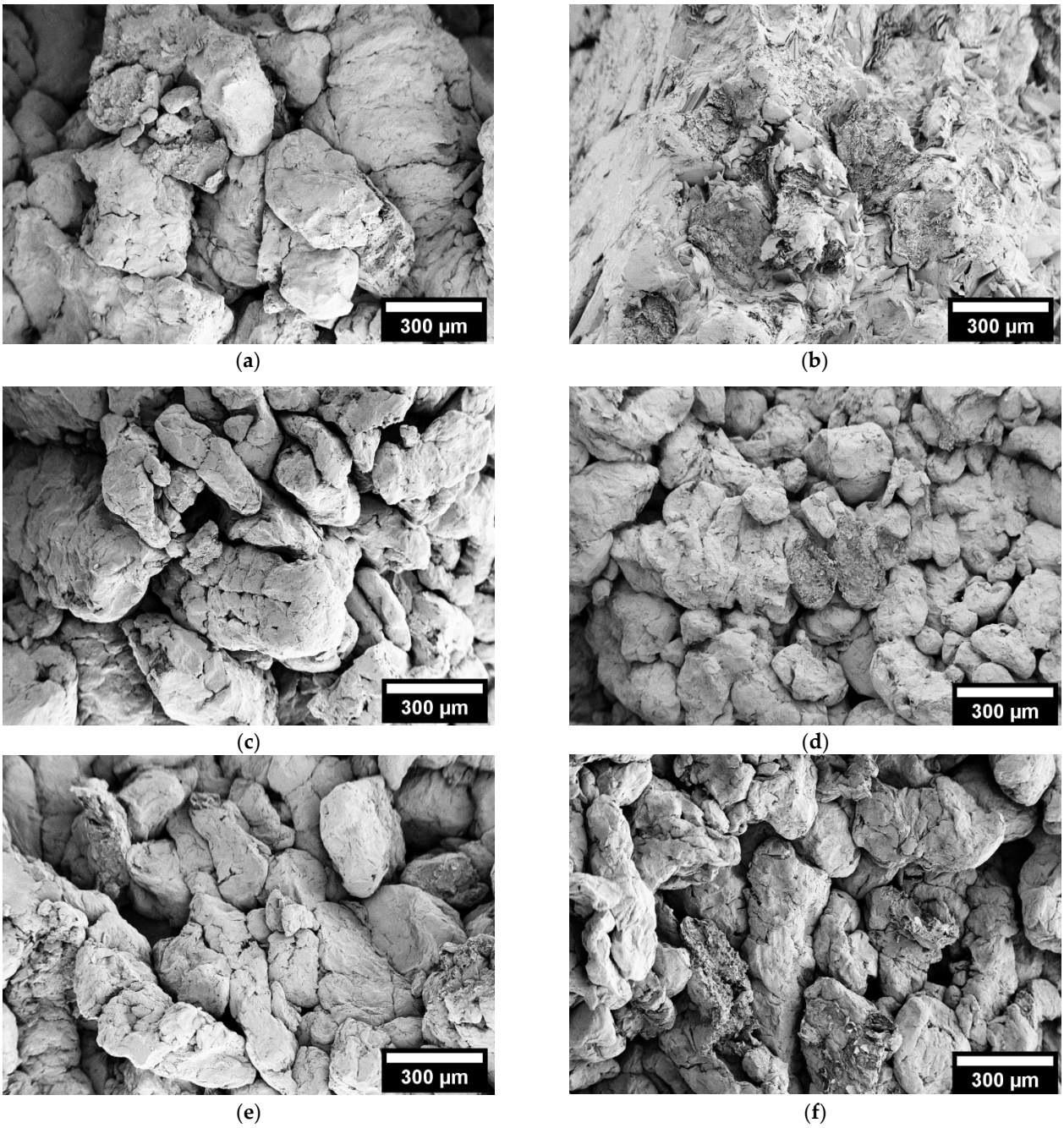

Figure 11. Low-magnification micrographs of compacted PA-SA/EG samples at 25 °C before melting and after one melting: (**a**) PA-SA/EG10 before melting; (**b**) PA-SA/EG10 after melting; (**c**) PA-SA/EG12 before melting; (**d**) PA-SA/EG12 after melting; (**e**) PA-SA/EG14 before melting; (**f**) PA-SA/EG14 after melting.

This low magnification gives an overview of the composite materials' morphologies; single powdery granules, that are able to adhere to each other due to weak interactions and mechanical interlocking after cold compaction, are recognizable. After melting, in particular for the PA-SA/EG10 sample (Figure 11b), the PCM escapes from the EG matrix, acting as a binder between the granules; this behaviour is confirmed by handling the

samples that, after a thermal cycle above 60 °C, become less friable. After PA-SA melting, fracture surfaces of the granules can be observed, whereas before melting, the fracture occurs between the powder particles. Hence, during the production process, a thermal cycle above the PA-SA melting point can be useful to obtain a more resistant composite material, reducing the risks to break the panel before the PE envelope thermo-welding operation. Moreover, the morphology is found to be homogeneous for all the three compositions, although the PA-SA/EG10 has an excessive PCM content which is not entrapped into the interconnected EG porosity, as observed from the leaking test.

In Figure 12, SEM micrographs are shown at higher magnification in order to help better recognize morphological features.

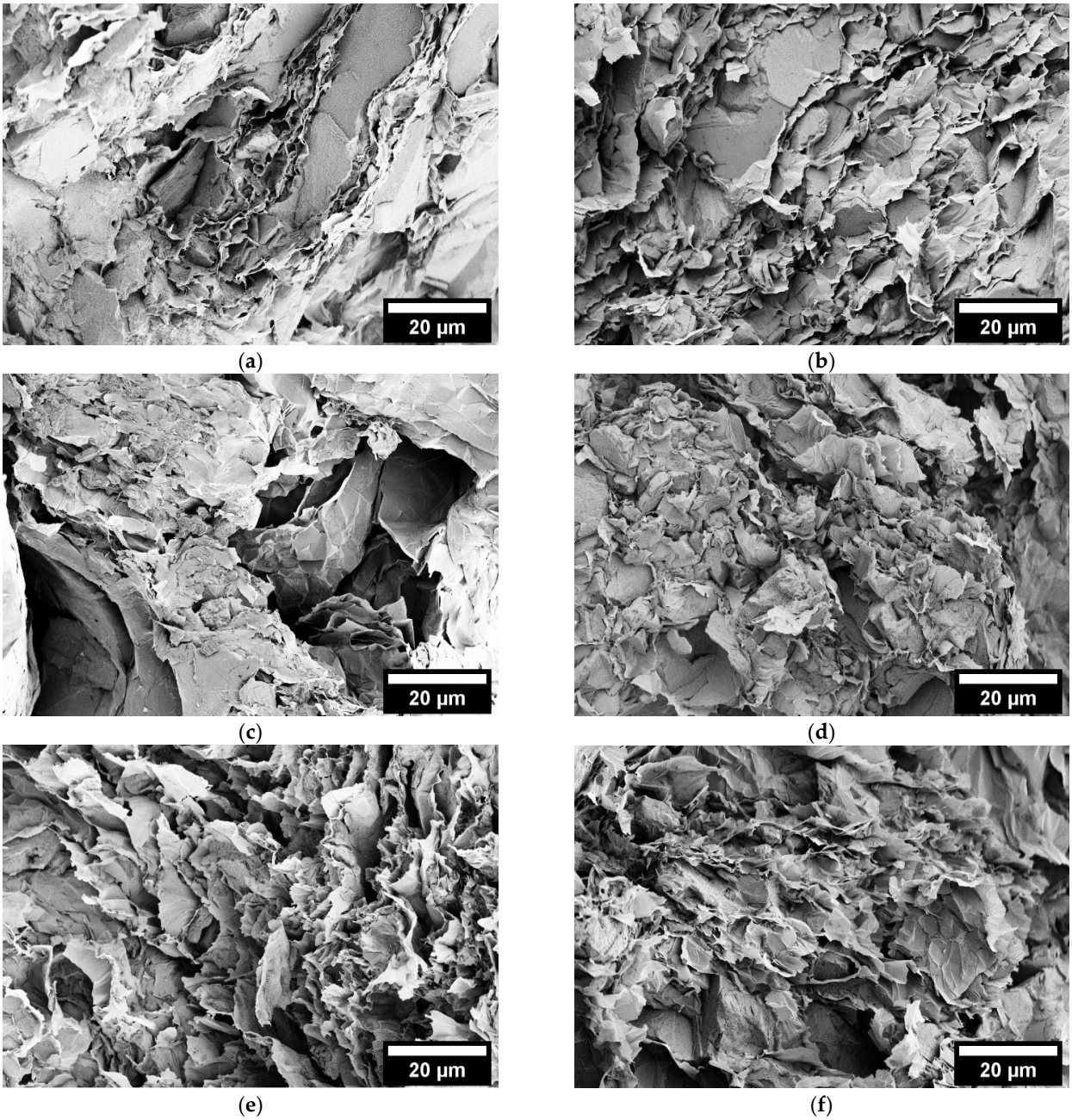

Figure 12. High-magnification micrographs of compacted PA-SA/EG samples at 25 °C before melting and after one melting: (**a**) PA-SA/EG10 before melting; (**b**) PA-SA/EG10 after melting; (**c**) PA-SA/EG12 before melting; (**d**) PA-SA/EG12 after melting; (**e**) PA-SA/EG14 before melting; (**f**) PA-SA/EG14 after melting.

The lamellar structure of graphite having a high surface area, among which PA-SA intercalates and stabilizes itself, and which is entrapped within the matrix due to the surface tension effect and capillary forces can be observed. No phase separation clearly appears, which determines high stability. These SEM observations and derived microstructural behaviour are in accordance with the studies of Li et al. [39], Wu et al. [41] and Zhang et al. [44]. A high interconnection of EG flakes is recognizable, forming a graphitic network in which the PCM is intercalated. Moreover, when the EG content is increased, the material appears more homogeneous.

3.7. Specific Heat Capacity

Specific heat capacity is a fundamental property of PCM-based materials, giving complementary information to transition enthalpy to determine the heat storage behaviour and evaluate the thermal conductivity. The obtained c_p values at 30 °C and 80 °C for PA-SA and the composite systems are reported in Table 8.

Table 8. Evaluated specific heat capacity on neat PA-SA and disks having a density of 1 g/cm^3 at 30 °C and 80 °C.

Sample	c_{p30} [J/(g K)]	c_{p80} [J/(g K)]
PA-SA	2.11 ± 0.09	2.30 ± 0.06
PA-SA/EG10	1.97 ± 0.13	2.20 ± 0.13
PA-SA/EG12	1.94 ± 0.08	2.16 ± 0.09
PA-SA/EG14	1.93 ± 0.09	2.17 ± 0.09

A slightly decreasing trend in c_p values with EG addition can be noticed. The trend is coherent to that found by Wang et al. [31]. The obtained values are slightly lower than those of the compared work because the analysed fatty acid mixtures were different and the transition onset was below 30 °C; hence, only a comparison at different temperatures could be performed. The c_p values increase by around 0.2 J/(g K) when passing from the PCM solid state at 30 °C to the liquid one at 80 °C.

3.8. Thermal Conductivity

High thermal conductivity is a fundamental property that must be guaranteed to a bulk TMS in order to permit a proper heat transfer to the PCM, whose thermal conductivity is 0.2 W/(m K) from the datasheet. In Figure 13, the thermal conductivity values at 30 °C from both hot disk and LFA techniques for the EG-stabilized PA-SA as a function of geometrical density and EG content are reported.

From Figure 13, the linear increase in thermal conductivity as a function of density is evident. This is in accordance with Equation (6); thus, a denser material possesses a higher thermal conductivity, considering the constant c_p and α affected by void fraction. Moreover, a beneficial effect in the improvement of thermal conductivity by increasing the EG content is clearly evident when passing from 10 phr to 12 phr rather than from 12 phr to 14 phr. This is one of the objectives of the PCM stabilization with a carbon-based matrix, whose effect in increasing thermal conductivity and diffusivity is confirmed by many studies on PA-SA/EG systems, with a threshold of around 10–15 wt% EG, above which the increase in thermal conductivity is less pronounced [55–57].

The improvement in thermal conductivity is thence more relevant when increasing the compaction of the powder than when exceeding with the EG content [41]. However, limits in the cold compaction process must be considered due to the high pressures necessary to overcome 0.94 g/cm^3, for 14 phr EG content, 0.93 g/cm^3 for 12 phr and 0.92 g/cm^3 for 10 phr, which are considered as the threshold in this work to obtain blocks suitable for PV cells. At these densities, the obtained λ_{HD} values that can be extrapolated from the curves are 4.6 W/(m K) for PA-SA/EG10, 7.5 W/(m K) for PA-SA/EG12 and 8.3 W/(m K) for PA-SA/EG14, hence 40 times more with respect to the neat PCM, that is about 0.2 W/(m K)

according to the literature [31,41,50]. These values can be increased up to 5.2 W/(m K) for PA-SA/EG10, 8.3 W/(m K) for PA-SA/EG12 and 9.2 W/(m K) for PA-SA/EG14 by increasing the compaction density to 1 g/cm^3. The thermal conductivity of pressed EG having a bulk density of 1.90 g/cm^3 (Figure S1), evaluated through LFA, was 25.60 ± 0.03 W/(m K).

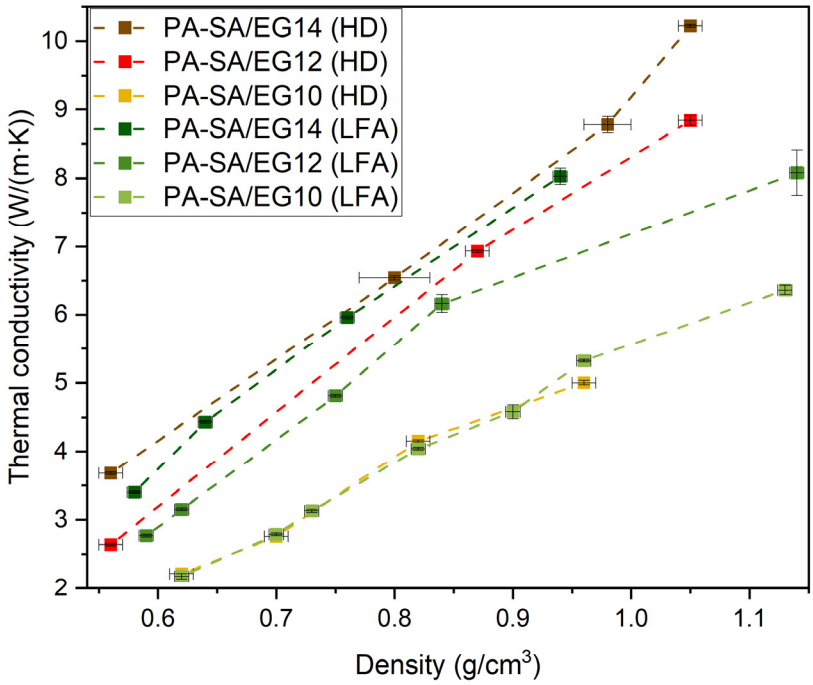

Figure 13. Thermal conductivity values of PA-SA/EG systems as a function of bulk density evaluated using hot disk (HD) and LFA techniques at 30 °C.

The use of rotavapor preparation followed by compression moulding allows us to obtain higher thermal conductivity values than those obtained via melt impregnation considering the same EG content [24–26], also in the case of an additional contribution of an aluminium honeycomb structure [50]. Much higher values only in a preferential direction can be obtained by pressing graphite layers using 25 wt.% EG, obtaining a laminar structure having an anisotropic thermal conductivity, reaching values higher than 20 W/(m K) in the radial direction at a density higher than 0.8 g/cm^3, as obtained by Wu et al. [41]; this result confirmed the quality of the pressed EG measurement obtained using LFA. Thermal conductivity can be further increased by selecting higher EG fractions, obtaining as a second advantage an improvement in leaking resistance at the expense of enthalpy and thus the ability to subtract heat for unit of mass. In addition, significantly exceeding the EG content (20 wt.% or more) may lead to compaction problems due to the formation of cracks in the plates just after tens of thermal cycles [41].

A limited difference between the values found using hot disk and LFA techniques is evident; these discrepancies are not so marked and are acceptable in the present study: for the case of 10 phr, the two curves well overlap; at 14 phr, the differences are in the order of 0.1 W/(m K); while in the case of 12 phr, the differences are higher, especially above 0.8 g/cm^3. Sources of errors could be inhomogeneities of the tested material, i.e., imprecisions in the determination of bulk density and in the case of hot disk tests, in which the sensor was stuck between two different specimens. The calibration of the pressure to be applied in order to obtain the proper density of a small disk was not easy; thus, some measurements cannot be precise if the densities of the two specimens were too different. These aspects are quite common when thermal conductivity tests are performed, as noticed and extensively treated by Weingrill et al. [58].

Finally, the role of the PE film used as an external envelope had to be considered. It possessed λ in the order of 0.5 W/(m K); however, due to the low thickness (95 μm), the

thermal barrier effect can be considered to be not detrimental for the thermal response of the multilayer material. In the case of PA-SA/EG14, when simplifying the heat transmission for conduction only in the direction perpendicular to the thickness, the conductive thermal resistance of the PE envelope was only 0.05 K/W, a contribution that can be linearly added to the 0.59 K/W of the brick with a thickness of 2 cm. Moreover, for real applications, it is essential to guarantee a good contact between the PCM-based composite material and the PV cell in order to guarantee the heat transfer with a thermal conduction mechanism; otherwise, a thin layer of air can behave as an undesired thermal insulation barrier.

3.9. Test in Climatic Chamber

From the results of the leakage and thermal conductivity tests, PA-SA/EG14 is selected as the best composition for PCM stabilization. The further characterizations were performed only for this optimized sample. In Figure 14, the temperature profiles of the PA-SA/EG14 bricks having three different masses (12 g, 66 g and 92 g), thicknesses (10 mm, 17 mm and 25 mm) and surface densities (9.4 kg/m^2, 5.3 kg/m^2 3.8 kg/m^2) subjected to the thermal cycles of the three coldest and hottest days of summer 2022 for the cities of Verona and Gela are reported. The recorded air temperature simulates the temperature reached by the PV cell inclined at 30° with respect to the horizontal. The temperature of the glass base sheet supporting the specimens is also reported for a comparative evaluation.

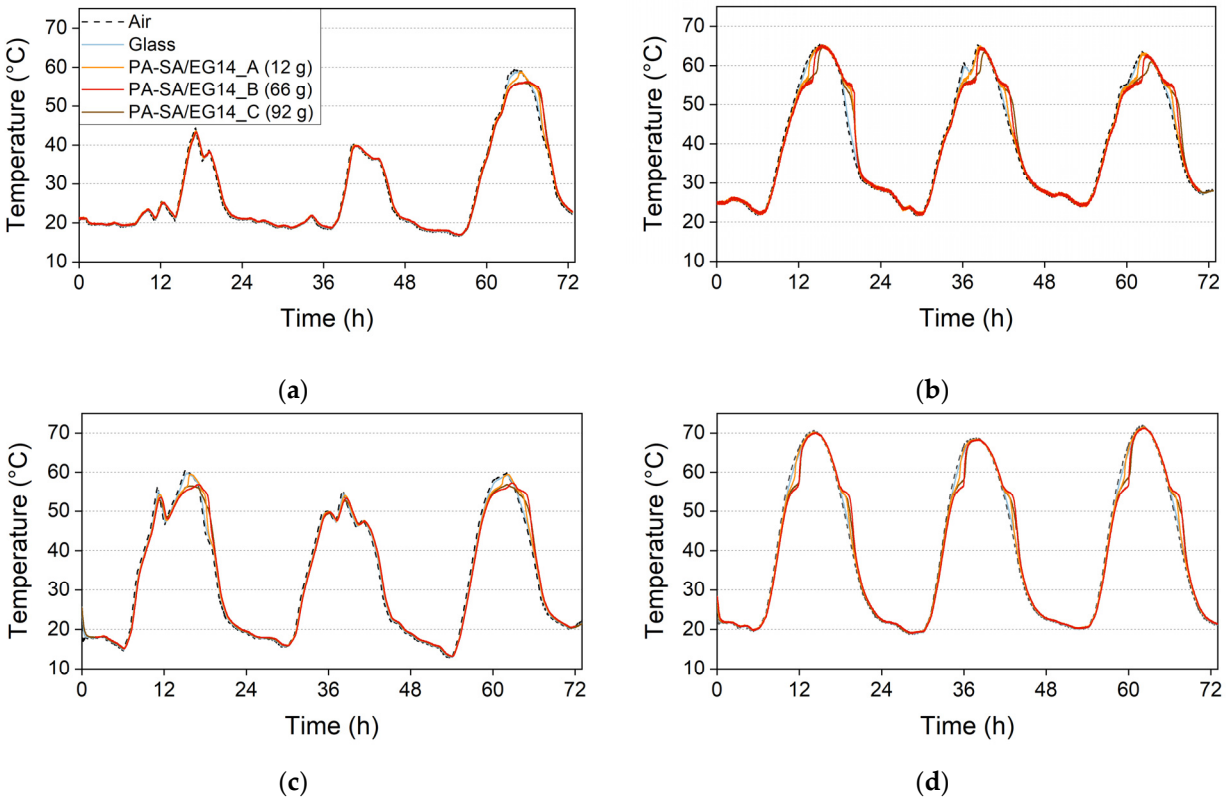

Figure 14. Climatic chamber simulations with PA-SA/EG14 bricks at different masses (12 g, 66 g and 92 g) and thicknesses (10 mm, 17 mm and 25 mm) in different conditions: (**a**) three coldest days in Verona; (**b**) three hottest days in Verona; (**c**) three coldest days in Gela; (**d**) three hottest days in Gela. For further details, see Tables S3–S6.

Observing the curves shown in Figure 14a, no PCM melting can be noticed in the first two coldest days due to the low reached temperatures, so the maximum and minimum temperatures are similar for all the specimens. During the third day, the thermal management mechanism is activated, and in particular, for the specimens with masses higher than 66 g, the amount of PCM is sufficient to completely avoid reaching the peak temperature,

decreasing it of 3 °C (Table S3). This is an example of a proper calibration of the enthalpy required for the TMS, with a fraction of PCM which never melts unless in the hottest days for a few hours in an entire year. During cooling, the delay in reaching 53 °C with respect to the environment for all the samples is close to 1 h (Table S3).

In the three hottest days in Verona (Figure 14b), PA-SA melts with a delay effect in the temperature increase after melting that can be quantified in 1 to 3 h, depending on the mass (Table S4), with the maximum temperature decreasing to just tenths of degrees (always higher than 65 °C). This behaviour is similar to that in the three hottest days in Gela (Figure 14d, Table S6). During crystallization, this delay occurs as well, but at lower temperatures and for a lower time, guaranteeing a total balance in the reached temperatures with a potential time benefit for PV efficiency.

For the first of the three coldest days in Gela (Figure 14c), the thermal management mechanism is activated and, with sufficient mass (at least 66 g for the considered test), it is able to maintain the peak temperature 3.8 °C below the imposed one (Table S5) with a behaviour similar to that observed in Figure 14a. During the second day, the temperatures are too low to melt the PA-SA, while in the third day, the thermal management provides a delay in reaching the maximum temperature in the case of sample A and a peak temperature reduction of 2.8 °C for sample C (Table S5).

Finally, the minimum temperatures in all the 12 simulated days present no significant variations with respect to the values reached by the glass. This is an advantage because it means that during the night, the release of the stored heat occurs completely with crystallization and there is enough time for the material to stabilize its temperature with the environment, thereby guaranteeing the minimum possible temperature when the temperature starts to rise at the beginning of the day.

The tested blocks present good reliability with a good maintenance of their shape, as shown in Figure 15, with no presence of cracks (as contrarily experienced in a similar work at higher EG fractions [41]). High reliability is also experienced in other studies after 100 [53] to 500 cycles [30].

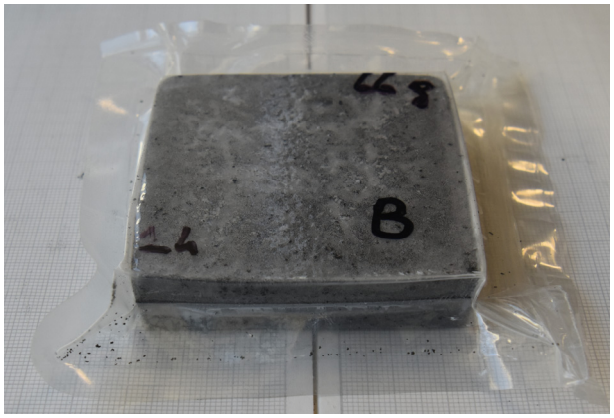

Figure 15. One of the tested blocks after 30 melting/crystallization thermal cycles.

3.10. Mechanical Properties

The TMS blocks were tested under compression to quantify a pressure which can be applied to maintain their attachment on the rear of the PV cells. In Figure 16, a representative compression stress–strain curve for the PA-SA/EG14 sample at 30 °C and 80 °C is reported, while in Table 9, the characteristic parameters at 30 °C and 80 °C are listed.

From the results at 30 °C, a quite strong and rigid behaviour of the material can be noticed, hence the bricks can be subjected to pressures higher than 1 MPa without shape stability problems below the PA-SA melting point. At 80 °C a decrease of one order of magnitude in the applicable stress occurs alongside an evident increase in strain at break. This is due to the very abundant leakage of molten PA-SA, which is squeezed out to the EG matrix once a pressure is applied. The first portion of the curves in which the strain

increases without a relevant detection of stresses can be attributed to the compensations of the testing instrumentation and to the eventual accommodation of the PE film. At 80 °C, the compressive modulus is drastically reduced by about 20 times due to the very high fraction of PCM squeezed out under load. After the application of 0.2 MPa, the PCM leakage occurs and the test ends with the break of the PE envelope and PCM wetting of the lower plate of the machine.

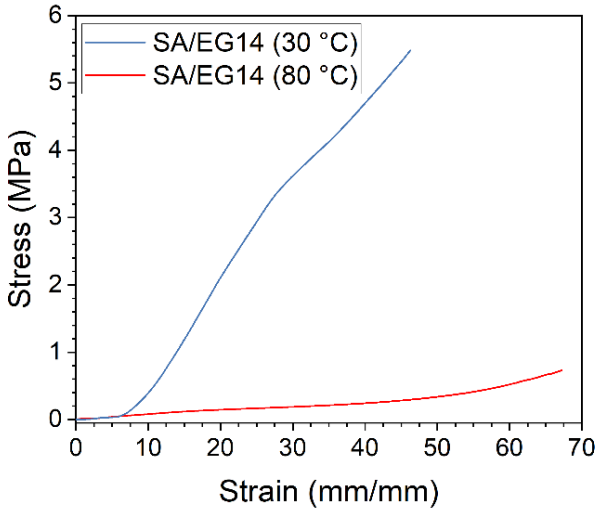

Figure 16. Stress–strain curve of compression test for PA-SA/EG14 sample (40 × 40 × 10 mm^3) at 30 °C and at 80 °C.

Table 9. Results of PA-SA/EG14 compression tests at 30 °C and 80 °C.

T [°C]	E_C [MPa]	σ_{10} [MPa]	σ_{20} [MPa]	$\varepsilon_{0.5}$ [%]	ε_5 [%]
30	16.0 ± 8.0	0.7 ± 0.4	2.4 ± 0.5	9.0 ± 2.0	40.8 ± 1.9
80	0.72 ± 0.06	0.082 ± 0.002	0.143 ± 0.004	58.8 ± 0.6	-

In Figure 17, a picture of two specimens of PA-SA/EG14 tested at 30 °C and 80 °C can be observed, underlying the spreading of the material tested at 80 °C with a complete destruction of the specimens. At 30 °C, all the envelopes remain without any damage after the tests.

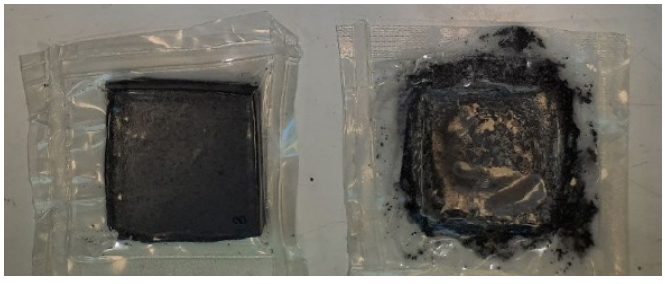

Figure 17. Tested enveloped PA-SA/EG14 samples under compression at 30 °C (**left**) and 80 °C (**right**).

For real applications, a lateral containment of the material is needed to preserve the shape and structural integrity of the systems above the PA-SA melting point.

3.11. Enveloped Sheet Behaviour at 60 °C

In Figure 18, enveloped PA-SA/EG specimens heated in an oven at 60 °C are shown. The sheets, having a thickness of 3 mm, deflect under the action of their own weight, and in a more evident manner particularly for the 10 phr EG content.

(**a**) (**b**)

Figure 18. (**a**) Enveloped PA-SA/EG sheets from left to right 14, 12, 10 phr (effect of bending at 60 °C—angle 45°); (**b**) enveloped PA-SA/EG10 flexibility at 60 °C.

A change in the behaviour of the PA-SA/EG samples appears evident: at room temperature, the sheets present themselves as rigid and brittle, while at 60 °C, they become flexible. This behaviour can be explained by the plasticizing effect of the molten PCM among the EG particles, which in crystallized form is rigid and brittle.

3.12. Optimum Selected System Summary

In Table 10, the characteristics of the PA-SA/EG14 sample, selected as the best candidate for the TMS realization due to the compromise between enthalpy, high thermal conductivity and PCM stabilization, are summarized.

Table 10. Specifics of optimum TMS.

TMS Bricks	ρ [g/cm^3]	SD [kg/m^2]	c_{p30} [J/(g K)]	λ_{30} [W/(m K)]	T_m [°C]	T_c [°C]	ΔH_m [J/g]	TMA [MJ/m^2]
PA-SA/EG14	0.94	18.8	1.93	8.3	53.6	50.7	169	3.2

ρ = density, SD = surface density of a panel 2 cm thick, c_{p30} = the specific heat capacity at 30 °C, λ_{30} = thermal conductivity at 30 °C, T_m = melting temperature, T_c = crystallization temperature, ΔH_m = melting enthalpy, TMA = thermal management ability of a system 2 cm thick and normalized to the surface, which corresponds to the heat that the device is able to remove from the PV cell.

4. Conclusions

Expanded graphite (EG) was successfully used to stabilize a mixture of stearic and palmitic acid for thermal management applications. In particular, the behaviour of a PCM having melting temperatures close to 53 °C and a melting enthalpy of 196 J/g has been shape-stabilized with EG, using a strategy that is able to improve the thermal conductivity, and finding the optimal amount of EG at 14 phr.

The result is an homogeneous system having a density of 0.94 g/cm^3, melting enthalpy of 169 J/g and thermal conductivity of 8.3 W/(m K), which can be enhanced till 9 W/(m K), increasing the density by applying a higher pressure in the cold compaction process. The obtained enthalpy is higher than the majority of works present in the literature, exploiting PA-SA mixtures; hence, the investigated systems can be considered particularly suitable for heat subtraction in thermal management applications at 53 °C.

A good compromise between high PCM content and leakage resistance was found by fixing the amount of EG at 14 phr (12.3 wt.%), underlying its capability to be used as a filler in skeletons in PCM-based composites. In this study, a thermo-welded PE envelope around the TMS blocks is necessary to safely contain the material without dispersions in the environment. Moreover, the thermal conductivity of the composite was extraordinarily high, about 40 times more with respect to the neat PCM.

From the simulation of temperatures inside the climatic chamber, reached by the PV cells in Verona and Gela and referring to summer 2022 temperatures, thermal management effects with delays in temperature increase are confirmed for the hottest days, while reductions in daily peak temperatures are guaranteed only for days with intermediate temperatures. These results can suggest the study of lower-melting-point PCMs for the thermal management of PV cells.

This research detailed the production and the properties of various compositions of PCM systems with EG content in the range 10–14 phr, with a good leakage stability and a TMA value of 3.2–3.4 MJ/m^2, offering a proper compromise between transition enthalpy and thermal conductivity. The critical temperature to avoid or limit the dramatic reduction in the efficiency was set at 60 °C, and the selection of the PCMs was performed by searching for melting temperature peaks slightly lower than 55 °C. On the other hand, for a better thermal management action, PCMs with lower melting temperatures should be properly selected and prepared. In conclusion, these composite blends of stearic and palmitic acid stabilized with EG, compared with other PCM materials, evidenced high stability, good cost-effectiveness and good scalability.

Future work will be devoted to the selection of PCMs as a function of the region where the PV panel will be installed, calibrating the melting point and the amount of material on the basis of the available environmental data, and optimizing the EG content in order to find the best compromise between costs and thermal properties.

Supplementary Materials: The following supporting information can be downloaded at: https://www.mdpi.com/article/10.3390/c10020046/s1, Figure S1: Pressed EG disks of 13.0 mm in diameter for the evaluation of density. On the left, density is 1.87 g/cm3 (2.274 g, thickness 9.16 mm); on the right, density is 1.90 g/cm3 (0.823 g and 3.27 mm thick); Figure S2: TGA curves in air atmosphere: (a) residual mass; (b) derivative of mass loss (DTGA); Table S1: Selected results of TGA and DTGA analyses in air; Table S2: Results of DSC tests at 0.1 °C/min, 1 °C/min and 10 °C/min of neat PA-SA; Figure S3: Climatic chamber simulations with PA-SA/EG14 bricks during the three coldest days in Verona: 18 August 2022–19 August 2022–20 August 2022; Table S3: Characteristic times and temperatures for the reproduction of the three coldest days in Verona: 18 August 2022–19 August 2022–20 August 2022; Figure S4: Climatic chamber simulations with PA-SA/EG14 bricks during the three hottest days in Verona: 22 July 2022–23 July 2022–24 July 2022; Table S4: Characteristic times and temperatures for the reproduction of the three hottest days in Verona: 22 July 2022–23 July 2022–24 July 2022; Figure S5: Climatic chamber simulations with PA-SA/EG14 bricks during the three coldest days in Gela: 08 June 2022–09 June 2022–10 June 2022; Table S5: Characteristic times and temperatures for the reproduction of the three coldest days in Gela: 08 June 2022–09 June 2022–10 June 2022; Figure S6: Climatic chamber simulations with PA-SA/EG14 bricks during the three hottest days in Gela: 26 June 2022–27 June 2022–28 June 2022; Table S6: Characteristic times and temperatures for the reproduction of the three hottest days in Gela: 26 June 2022–27 June 2022–28 June 2022; Table S7: Property comparison of thermal management systems.

Author Contributions: Conceptualization, S.S., F.V., L.F. and R.P.; methodology, S.S., F.V., L.F., A.B., M.G. and R.P.; validation, S.S., R.P. and L.F.; formal analysis, S.S.; investigation, S.S.; resources, L.F.; data curation, S.S.; writing—original draft preparation, S.S., R.P. and M.G.; writing—review and editing, F.V., L.F. and R.P.; supervision, F.V., R.P. and L.F.; project administration, R.P. and L.F. All authors have read and agreed to the published version of the manuscript.

Funding: This research received no external funding.

Data Availability Statement: The raw data supporting the conclusions of this article will be made available by the authors on request.

Acknowledgments: Alfredo Casagranda and Claudia Gavazza are gratefully acknowledged for their help in the experimental work.

Conflicts of Interest: Authors Alice Benin, Marco Guidolin, and Riccardo Po were employed by the company Eni S.p.A. The remaining authors declare that the research was conducted in the absence of any commercial or financial relationships that could be construed as a potential conflict of interest.

References

1. Kaldellis, J.K.; Kapsali, M. Temperature and wind speed impact on the efficiency of PV installations. Experience obtained from outdoor measurements in Greece. *Renew. Energy* **2014**, *66*, 612–624. [CrossRef]
2. Dwivedi, P.; Sudhakar, K. Advanced cooling techniques of P.V. modules: A state of art. *Case Stud. Therm. Eng.* **2020**, *21*, 100674. [CrossRef]
3. Mehling, H.; Brütting, M. PCM products and their fields of application—An overview of the state in 2020/2021. *J. Energy Storage* **2022**, *51*, 104354. [CrossRef]
4. Song, M.; Niu, F. Review on building energy performance improvement using phase change materials. *Energy Build.* **2018**, *158*, 776–793. [CrossRef]
5. Frigione, M.; Lettieri, M. Phase Change Materials for Energy Efficiency in Buildings and Their Use in Mortars. *Materials* **2019**, *12*, 1260. [CrossRef] [PubMed]
6. Liu, C.; Xu, D. Phase Change Materials Application in Battery Thermal Management System: A Review. *Materials* **2020**, *13*, 4622. [CrossRef] [PubMed]
7. Nižetić, S.; Arıcı, M. Investigation of pork fat as potential novel phase change material for passive cooling applications in photovoltaics. *J. Clean. Prod.* **2018**, *170*, 1006–1016. [CrossRef]
8. Browne, M.C.; Norton, B. Phase change materials for photovoltaic thermal management. *Renew. Sustain. Energy Rev.* **2015**, *47*, 762–782. [CrossRef]
9. Dupré, O.; Vaillon, R. Physics of the temperature coefficients of solar cells. *Sol. Energy Mater. Sol. Cells* **2015**, *140*, 92–100. [CrossRef]
10. Chang, C.; Nie, X. Bioinspired roll-to-roll solar-thermal energy harvesting within form-stable flexible composite phase change materials. *J. Mater. Chem. A* **2020**, *8*, 20970–20978. [CrossRef]
11. Singh, P.; Sharma, R.K. Evaluation of carbon based-supporting materials for developing form-stable organic phase change materials for thermal energy storage: A review. *Sol. Energy Mater. Sol. Cells* **2022**, *246*, 111896. [CrossRef]
12. Singh, P.; Sharma, R.K. A comprehensive review on development of eutectic organic phase change materials and their composites for low and medium range thermal energy storage applications. *Sol. Energy Mater. Sol. Cells* **2021**, *223*, 110955. [CrossRef]
13. Kumar, K.; Sharma, K. Experimental Investigation of Graphene-Paraffin Wax Nanocomposites for Thermal Energy Storage. *Mater. Today Proc.* **2019**, *18*, 5158–5163. [CrossRef]
14. Mehrali, M.; Latibari, S.T. Shape-stabilized phase change materials with high thermal conductivity based on paraffin/graphene oxide composite. *Energy Convers. Manag.* **2013**, *67*, 275–282. [CrossRef]
15. Kuziel, A.W.; Dzido, G. Ultra-long carbon nanotube-paraffin composites of record thermal conductivity and high phase change enthalpy among paraffin-based heat storage materials. *J. Energy Storage* **2021**, *36*, 102396. [CrossRef]
16. Cai, Z.; Liu, J. Flexible phase change materials with enhanced tensile strength, thermal conductivity and photo-thermal performance. *Sol. Energy Mater. Sol. Cells* **2021**, *219*, 110728. [CrossRef]
17. Rathore, P.K.S.; Shukla, S.K. Potential of macroencapsulated PCM for thermal energy storage in buildings: A comprehensive review. *Constr. Build. Mater.* **2019**, *225*, 723–744. [CrossRef]
18. Jamekhorshid, A.; Sadrameli, S.M. A review of microencapsulation methods of phase change materials (PCMs) as a thermal energy storage (TES) medium. *Renew. Sustain. Energy Rev.* **2014**, *31*, 531–542. [CrossRef]
19. Hong, Y.; Ge, X.-S. Preparation of polyethylene–paraffin compound as a form-stable solid-liquid phase change material. *Sol. Energy Mater. Sol. Cells* **2000**, *64*, 37–44. [CrossRef]
20. Krupa, I.; Miková, G. Polypropylene as a potential matrix for the creation of shape stabilized phase change materials. *Eur. Polym. J.* **2007**, *43*, 895–907. [CrossRef]
21. Kaygusuz, K.; Alkan, C. Encapsulated Fatty Acids in an Acrylic Resin as Shape-stabilized Phase Change Materials for Latent Heat Thermal Energy Storage. *Energy Sources Part A Recovery Util. Environ. Eff.* **2008**, *30*, 1050–1059. [CrossRef]
22. Wu, T.; Hu, Y. SEBS-based composite phase change material with thermal shape memory for thermal management applications. *Energy* **2021**, *221*, 119900. [CrossRef]
23. Valentini, F.; Dorigato, A. Production and characterization of novel EPDM/NBR panels with paraffin for potential thermal energy storage applications. *Therm. Sci. Eng. Prog.* **2022**, *32*, 101309. [CrossRef]
24. Ao, C.; Yan, S. Stearic acid/expanded graphite composite phase change material with high thermal conductivity for thermal energy storage. *Energy Rep.* **2022**, *8*, 4834–4843. [CrossRef]
25. Gao, H.; Bing, N. Energy harvesting and storage blocks based on 3D oriented expanded graphite and stearic acid with high thermal conductivity for solar thermal application. *Energy* **2022**, *254*, 124198. [CrossRef]
26. Karaipekli, A.; Sarı, A. Thermal conductivity improvement of stearic acid using expanded graphite and carbon fiber for energy storage applications. *Renew. Energy* **2007**, *32*, 2201–2210. [CrossRef]
27. Zhao, J.; Lv, P. Experimental study on the thermal management performance of phase change material coupled with heat pipe for cylindrical power battery pack. *Exp. Therm. Fluid Sci.* **2017**, *82*, 182–188. [CrossRef]
28. Wu, W.; Wu, W. Form-stable and thermally induced flexible composite phase change material for thermal energy storage and thermal management applications. *Appl. Energy* **2019**, *236*, 10–21. [CrossRef]
29. Wu, S.; Yan, T. Thermal conductivity enhancement on phase change materials for thermal energy storage: A review. *Energy Storage Mater.* **2020**, *25*, 251–295. [CrossRef]

30. Liu, S.; Zhang, X. A Low-Temperature Phase Change Material Based on Capric-Stearic Acid/Expanded Graphite for Thermal Energy Storage. *ACS Omega* **2021**, *6*, 17988–17998. [CrossRef]
31. Wang, Z.; Huang, G. Eutectic Fatty Acids Phase Change Materials Improved with Expanded Graphite. *Materials* **2022**, *15*, 6856. [CrossRef]
32. Chen, Y.; Gao, S. Preparation of PE-EPDM based phase change materials with great mechanical property, thermal conductivity and photo-thermal performance. *Sol. Energy Mater. Sol. Cells* **2019**, *200*, 109988. [CrossRef]
33. Sarı, A.; Karaipekli, A. Preparation, thermal properties and thermal reliability of palmitic acid/expanded graphite composite as form-stable PCM for thermal energy storage. *Sol. Energy Mater. Sol. Cells* **2009**, *93*, 571–576. [CrossRef]
34. Dai, J.; Ma, F. Optimization and characterization of fatty acids based ternary eutectic phase change system. *J. Mol. Liq.* **2024**, *396*, 123975. [CrossRef]
35. Shi, Y.; Zhao, Y. Study on the Reliability and Stability of Fatty Acid-Paraffin Ternary Phase Change Materials as Energy-saving Materials. *ChemistrySelect* **2024**, *9*, e202303114. [CrossRef]
36. Grzybek, J.; Nazari, M. Bio-based phase change material for enhanced building energy efficiency: A study of beech and thermally modified beech wood for wall structures. *Energy Storage* **2024**, *6*, e568. [CrossRef]
37. Dai, J.; Ma, F. Assessment of high-enthalpy composite eutectic phase change materials efficiency in asphalt binders for cooling pavements. *J. Clean. Prod.* **2024**, *442*, 140999. [CrossRef]
38. Fang, G.; Li, H. Preparation and characterization of stearic acid/expanded graphite composites as thermal energy storage materials. *Energy* **2010**, *35*, 4622–4626. [CrossRef]
39. Li, C.; Zhang, B. Stearic acid/expanded graphite as a composite phase change thermal energy storage material for tankless solar water heater. *Sustain. Cities Soc.* **2019**, *44*, 458–464. [CrossRef]
40. Zhang, J.-L.; Wu, N. High latent heat stearic acid impregnated in expanded graphite. *Thermochim. Acta* **2018**, *663*, 118–124. [CrossRef]
41. Wu, S.; Li, T.X. High performance form-stable expanded graphite/stearic acid composite phase change material for modular thermal energy storage. *Int. J. Heat Mass Transf.* **2016**, *102*, 733–744. [CrossRef]
42. Zukowski, M. Experimental study of short term thermal energy storage unit based on enclosed phase change material in polyethylene film bag. *Energy Convers. Manag.* **2007**, *48*, 166–173. [CrossRef]
43. Vohler, O.; Von Sturm, F. *Industrial Carbon and Graphite Materials*; John Wiley & Sons, Inc.: Hoboken, NJ, USA, 2021; Volume I.
44. Zhang, N.; Yuan, Y. Preparation and properties of palmitic-stearic acid eutectic mixture/expanded graphite composite as phase change material for energy storage. *Energy* **2014**, *78*, 950–956. [CrossRef]
45. *ASTM E1269-11*; Method for Determining Specific Heat Capacity by Differential Scanning Calorimetry. ASTM: West Conshohocken, PA, USA, 2018. Available online: https://www.astm.org/e1269-11.html (accessed on 9 May 2024).
46. *ISO 22007*; Plastics—Determination of Thermal Conductivity and Thermal Diffusivity. ISO: Geneva, Switzerland, 2022. Available online: https://www.iso.org/standard/81836.html (accessed on 9 May 2024).
47. Dhouib, A.; Filali, S. *Energy and the Environment*; Sayigh, A.A.M., Ed.; Pergamon: Oxford, UK, 1990.
48. Agenzia Regionale per la Prevenzione e Protezione Ambientale del Veneto. Available online: http://www.arpa.veneto.it/ (accessed on 4 September 2023).
49. Servizio Informativo Agrometeorologico Siciliano. Available online: http://www.sias.regione.sicilia.it/home.htm (accessed on 3 September 2023).
50. Liu, Z.; Huang, J. Preparation of SA–PA–LA/EG/CF CPCM and Its Application in Battery Thermal Management. *Nanomaterials* **2021**, *11*, 1902. [CrossRef]
51. Yu, H.; Gao, J. Preparation and properties of stearic acid/expanded graphite composite phase change material for low-temperature solar thermal application. *J. Therm. Anal. Calorim.* **2016**, *124*, 87–92. [CrossRef]
52. Tian, Y.; Zhang, N. Adsorption performance of expanded graphite and its binary composite microbeads toward oil and dyes. *Desalin. Water Treat.* **2020**, *178*, 283–295. [CrossRef]
53. Xu, L.; Yang, R. Stearic Acid/Inorganic Porous Matrix Phase Change Composite for Hot Water Systems. *Molecules* **2019**, *24*, 1482. [CrossRef]
54. Valentini, F.; Fambri, L. Production and Characterization of TES-EPDM Foams With Paraffin for Thermal Management Applications. *Front. Mater.* **2021**, *8*, 660656. [CrossRef]
55. Chriaa, I.; Karkri, M. The performances of expanded graphite on the phase change materials composites for thermal energy storage. *Polymer* **2021**, *212*, 123128. [CrossRef]
56. Li, C.; Zhang, B. N-eicosane/expanded graphite as composite phase change materials for electro-driven thermal energy storage. *J. Energy Storage* **2020**, *29*, 101339. [CrossRef]
57. Genito, T.M.; Dausen, D.F. Thermal management capability of phase change material in additively manufactured heat sinks. Master's Thesis, Naval Postgraduate School, Monterey, CA, USA, 2023.
58. Weingrill, H.; Hohenauer, W. Analyzing Thermal Conductivity of Polyethylene-Based Compounds Filled with Copper. *Macromol. Mater. Eng.* **2019**, *304*, 1800644. [CrossRef]